A multi-scale IMEX second order Runge-Kutta method for 3D hydrodynamic ocean models

Ange Pacifique Ishimwe[a], Eric Deleersnijder[b], Vincent Legat[a], Jonathan Lambrechts[a]

[a] *Université catholique de Louvain, Institute of Mechanics, Materials and Civil Engineering (IMMC), Avenue Georges Lemaître 4, B-1348 Louvain-la-Neuve, Belgium*
[b] *Université catholique de Louvain, Institute of Mechanics, Materials and Civil Engineering (IMMC) & Earth and Life Institute (ELI), Avenue Georges Lemaître 4, B-1348 Louvain-la-Neuve, Belgium*

Abstract

Understanding complex physical phenomena often involves dealing with partial differential equations (PDEs) where different phenomena exhibit distinct timescales. Fast terms, associated with short characteristic times, coexist with slower ones requiring relatively longer time steps for resolution. The challenge becomes more manageable when, despite the varying characteristic times of fast and slow terms, the computational cost associated with faster terms is significantly lower than that of slower terms. Additionally, slower terms can also exhibit two distinct longer characteristic times, adding complexity to the system and resulting in a total of three characteristic timescales. In this paper, an innovative split second-order IMEX (IMplicit-EXplicit) temporal scheme is introduced to address this temporal complexity. It is used to solve the primitive equation ocean model. Extremely short times are handled explicitly with small time steps, while longer timescales are managed explicitly and semi-implicitly using larger time steps. The decision to solve a portion of the slower terms semi-implicitly is due to the fact that it does not significantly increase the total computational cost, allowing for greater flexibility in the time step without imposing a substantial burden on the overall computational efficiency. This strategy enables efficient management of the various temporal scales present in the equations, thereby optimizing computational resources. The proposed scheme is applied to solve 3D hydrodynamics equations encompassing three time scale: fast terms representing wave phenomena, slow terms describing horizontal aspects and stiff terms for vertical ones. Furthermore, the scheme is designed to respect crucial physical properties, namely global and local conservation. The obtained results on different test cases demonstrate the robustness and efficiency of the IMEX approach in simulating these complex systems.

Keywords: split implicit-explicit Runge-Kutta, timestep methods, hydrodynamic equations, high order temporal scheme, primitive equation ocean model

1. Introduction

Numerical simulation plays a pivotal role in unraveling complex physical phenomena. By solving differential equations, these simulations facilitate the understanding of processes occurring from the ocean to the atmosphere, encompassing terrestrial dynamics. Previous studies have tackled challenges involved in formulating appropriate equations, selecting relevant parameters, determining characteristic values and defining boundary conditions.

The choice of a temporal scheme becomes challenging when dealing with equations that exhibit multiple timescales. These equations are categorized as stiff, signifying that at least one of their processes possesses a notably high characteristic velocity in comparison to the studied physical phenomena. For instance, this is prevalent in equations related to atmospheric dynamics or oceanic behaviors. Managing these equations often involves temporal schemes with exceedingly small time steps for resolving all terms during computations, but this approach incurs significant computational costs.

However, for specific problems, the troublesome terms have remarkably lower computational costs. This could be due to the fast terms being calculated across significantly fewer degrees of freedom than the slower terms. For such problems, a split temporal method becomes advantageous, allowing the computationally cheaper, fast terms to be computed numerous times compared to the computations of the computationally expensive, slower terms. In specific cases, within the slower terms, equations may exhibit phenomena with two distinct velocities. For instance, problems with exceptionally small aspect ratios exhibit this characteristic, as seen in oceanic models, where the vertical dimensions are significantly smaller than the horizontal ones. In these cases, the fast terms representing wave velocity are resolved in a two-dimensional grid, while the other terms with smaller characteristic velocities are handled in 3D. In oceanic or atmospheric models, the fast phenomena represent wave propagation. Due to the substantial aspect ratio, vertical phenomena within the slower terms tend to exhibit smaller characteristic timescales than horizontal phenomena. For instance, vertical diffusion, often arising from a turbulent closure model such as $k-\epsilon$ as described in (Rodi, 1987; Canuto et al., 2001), imposes more stringent constraints on the time step than horizontal diffusion.

To efficiently solve these equations, this paper introduces a second-order split implicit-explicit temporal scheme. Although this temporal scheme uses two well-known Runge-Kutta schemes, the resulting splitting is new. In addition, this scheme is novel in its application to ocean models on unstructured grids. The choice of second order is crucial in reducing the numerical dissipation of the overall scheme. For instance, in ocean applications, the numerical schemes used can introduce mixing rates of tracers and momentum than can be orders of magnitude larger than physical mixing (Burchard and Rennau, 2008; Rennau and Burchard, 2009; Hiester et al., 2014) . This is particularly true for the discretization of the horizontal advection (Marchesiello et al., 2009; Griffies et al., 2000), but it can arise from the vertical advection and diffusion as well (Shchepetkin A.F., 2005) or various filters introduced to improve numerical stability (Zhang et al., 2016). This numerical dissipation can be reduced by using higher order schemes.

In a prior publication, a fully explicit second-order split scheme is introduced, drawing inspiration from Wicker and Skamarock (2002); Wensch et al. (2009); Knoth and Wensch (2003). This schemes find application in atmospheric models, specifically handling terms in an explicit manner. Since the equations are predominantly influenced by advection terms, implicit treatment is not deemed necessary. Subsequent works by Nilsen and Loseth (1993); Visbal and Gaitonde (2002); Robert and Kaper (1986) introduce diffusion terms in splitting and treat them implicitly. However, the primary goal is not to create a final second-order temporal scheme; rather, the focus lies in achieving a direct low-storage implicit solution tailored to handle viscous terms. Essentially, the aim is to substantially minimize the computational effort associated with simulating turbulent flows with the larger time step possible.

While theoretically usable, the scheme detailed in Ishimwe et al. (2023) presentes challenges when transitioning to real-world scenarios due to the constraints imposed by vertical terms on the 3D time steps. Consequently, this paper introduces a semi-implicit facet to the stiff term, aiming to surmount the challenges encountered during realistic simulations and presents a comprehensive and practical scheme.

The temporal scheme is employed within the framework of 3D hydrodynamic equations and is implemented within the Second-generation Louvain-la-Neuve Ice-ocean Model (SLIM, www.slim-ocean.be). This software, developped in Louvain-la-Neuve through years as explained by (White et al., 2008; Blaise et al., 2010; Comblen et al., 2010), resolves them on unstructured grids. While structured grids are known for their great computational efficiency (Danilov et al., 2008; Danilov, 2013), unstructured meshes tend to be favored within coastal domains. This preference arises from their superior ability to accurately tackle intricate coastal topography and localized features (Deleersnijder and Lermusiaux, 2008; Pigott et al., 2013). The 3D mesh, composed of prisms, is obtained by extruding a 2D mesh of triangles. Typical approaches include terrain-following sigma-levels Blumberg and Mellor (1987); Pan et al. (2021), z-levels Griffies et al. (2005) and their generalization Song and Haidvogel (1994). Given the small aspect ratio of oceanic problems, the number of horizontal elements exceeds the number of vertical elements. For spatial discretization, SLIM employs the Discontinuous Galerkin method. This method discretizes the spatial fields using discontinuous Galerkin basis functions. As a result, at the boundaries between elements, the solution is discontinuous. The spatial discretization is shown in Appendix A (Ishimwe et al., 2023). This geometrical flexibility gives many advantages. Practically, this enables efficient numerical resolution, as each triangle, or prism in 3D, can solve its linear system without being blocked by other elements. This combines really well with the

split temporal scheme, as the fast terms are computed in a 2D grid, while the slow and stiff terms are computed in a 3D grid as explained by Kärnä et al. (2013). Even when deciding to resolve the vertical terms semi-implicitly, it does not diminish the method's effectiveness because the triangle-based systems become column-based systems for prisms. Furthermore, as mentioned earlier, the number of prisms per column is generally not excessive, ensuring these systems remain easily and efficiently solvable.

The structure of this article is as follows: it opens with an introduction to the hydrodynamic equations, highlighting their characteristic timescales. The subsequent section elaborates on the temporal scheme, detailing its construction, properties such as convergence order and the stability zone. Numerical results from diverse test cases are presented to effectively validate the model. Finally, the article concludes by summarizing the findings and implications of this study.

2. Governing physical equations

The temporal scheme outlined in this study is implemented in a coastal context, specifically targeting the three-dimensional hydrostatic equations derived from the Navier-Stokes equations. The study focus on three distinct timescale ranges: one short and two long timescales. Theses latter are due to the small aspect ratio of the domain, which is a common characteristic of coastal areas. The short timescale is associated with external gravity waves, while the two longer timescales are related to the horizontal and vertical dynamics.

2.1. Hydrodynamic equations

Given the Cartesian horizontal and vertical coordinates $\mathbf{x} = [x, y, z]^T$, the studied equations take the following form

$$\begin{aligned}\frac{\partial \mathbf{u}}{\partial t} + \boldsymbol{\nabla}_h \cdot (\mathbf{u}\mathbf{u}) + \frac{\partial (w\mathbf{u})}{\partial z} =& \boldsymbol{\nabla}_h \cdot (\nu_h \boldsymbol{\nabla}_h \mathbf{u}) + \frac{\partial}{\partial z}\left(\nu_v \frac{\partial \mathbf{u}}{\partial z}\right) \\ & - f\mathbf{e}_z \times \mathbf{u} - g\boldsymbol{\nabla}_h \eta - \frac{g}{\rho_0}\mathbf{q} - \frac{g}{\rho_0}\rho'|_\eta \boldsymbol{\nabla}_h \eta \qquad (1a)\\ \frac{\partial H}{\partial t} =& -\boldsymbol{\nabla}_h \cdot \int_{-b}^{\eta} \mathbf{u} dz \qquad (1b)\\ \frac{\partial w}{\partial z} =& -\boldsymbol{\nabla}_h \cdot \mathbf{u} \qquad (1c)\end{aligned}$$

In the provided equation set, ν_h, ν_v and $\boldsymbol{\nabla}_h$ respectively denote horizontal and vertical viscosity, which can be determined respectively by the Smagorinsky paramerisation (Smagorinsky, 1963; Blaise et al., 2007) and the $k-\epsilon$ turbulence closure model (Rodi, 1987; Kärnä, 2020) and the horizontal gradient. The horizontal velocity vector is denoted as $\mathbf{u} = (u,v)$, while w represents the vertical velocity. The variables $\mathbf{U} = \int_{-b}^{\eta} \mathbf{u} dz$ denote the total horizontal transport, where η and b stand for the free surface elevation and the bathymetry correspondingly. The column's height is symbolized by H and f denotes the Coriolis parameter. Additionally, $\mathbf{q}$ signifies the integral of the density deviation gradient, specifically defined as $\mathbf{q} = \int_z^{\eta} \boldsymbol{\nabla}_h \rho' d\zeta$. The density deviation relies on a state equation that depends on the water temperature or salinity (Jackett et al., 2006). They are modeled by the following advection-diffusion equations

$$\rho' = \rho'(T, S) \qquad (2)$$

$$\frac{\partial T}{\partial t} + \boldsymbol{\nabla}_h \cdot (\mathbf{u}T) + \frac{\partial (wT)}{\partial z} = \boldsymbol{\nabla}_h \cdot (\kappa_h \boldsymbol{\nabla}_h T) + \frac{\partial}{\partial z}\left(\kappa_v \frac{\partial T}{\partial z}\right) \qquad (3)$$

$$\frac{\partial S}{\partial t} + \boldsymbol{\nabla}_h \cdot (\mathbf{u}S) + \frac{\partial (wS)}{\partial z} = \boldsymbol{\nabla}_h \cdot (\kappa_h \boldsymbol{\nabla}_h S) + \frac{\partial}{\partial z}\left(\kappa_v \frac{\partial S}{\partial z}\right) \qquad (4)$$

κ_h and κ_v stand for respectively the horizontal and the vertical diffusivity.

The density deviation is defined as $\rho' = \rho - \rho_0$, where ρ_0 is the reference density.

Furthermore, SLIM tackles the equations within a three-dimensional domain Ω incorporating a free surface, managed using an Arbitrary Lagrangian-Eulerian (ALE) approach (Formaggia and Nobile, 2004). While the lateral boundary Γ_l and the bottom boundary Γ_b remain static, the surface boundary Γ_s dynamically moves over time, traversing the vertical coordinates between $z = -b$ and $z = \eta$. Impermeability conditions are imposed on both the top and bottom boundaries:

$$w + \mathbf{u} \cdot \boldsymbol{\nabla}_h b = 0 \qquad \mathbf{x} \in \Gamma_b \tag{5a}$$

$$w - \frac{\partial H}{\partial t} - \mathbf{u} \cdot \boldsymbol{\nabla}_h (H - b) = 0 \qquad \mathbf{x} \in \Gamma_s \tag{5b}$$

Also, a slip condition is implemented to accommodate bottom (Kärnä et al., 2013) and surface stresses, $\boldsymbol{\tau}_b$ and $\boldsymbol{\tau}_s$:

$$\nu_v \frac{\partial \mathbf{u}}{\partial z} = \frac{\boldsymbol{\tau}_b}{\rho_0} \qquad \mathbf{x} \in \Gamma_b \tag{6a}$$

$$\nu_v \frac{\partial \mathbf{u}}{\partial z} = \frac{\boldsymbol{\tau}_s}{\rho_0} \qquad \mathbf{x} \in \Gamma_s \tag{6b}$$

In the application of the temporal scheme to three-dimensional hydrodynamic equations, processes are grouped into three categories based on their timescales. Defining Δxy as the horizontal grid size and Δz as the vertical one enables to establish a value for the characteristic timescales. The following values are simplications as the real characteristic timescales are more complex depending from example of the spatial discritization. However, they are sufficient to understand the main idea of the method.

- **External gravity waves**, corresponding to the fastest phenomena, involve elevation gradient and water height evolution treated in a 2D grid allowing to conserve computational resources while requiring a smaller time step. Their characteristic timescale is defined as

$$\Delta t \propto \frac{\Delta xy}{\|\bar{\mathbf{u}}\| + \sqrt{gH}}$$

- **Vertical processes** are represented by the 3D semi-implicit terms. Given the equations' application in shallow areas, using 3D meshes with thin vertical layers, these terms exhibit reduced temporal characteristics, justifying their semi-implicit handling. These terms encompass the vertical advection, the vertical diffusion and the friction parametered with a quadratic function, split into linear components (vertical diffusion) and nonlinear components (vertical advection and friction). The quadratic bottom drag is defined :

$$\frac{\boldsymbol{\tau}_b}{\rho_0} = C_d |\mathbf{u}_b| \mathbf{u}_b$$

  where $\mathbf{u}_b$ is the horizontal velocity of the bottom element taken at the middle point and C_d is the drag coefficient. The characteristic timescale of these terms is

$$\Delta t \propto \max\left(\frac{\Delta z^2}{\nu_v}, \frac{\Delta z}{w}\right)$$

- **Horizontal processes** are treated explicitly. These terms include horizontal advection, horizontal diffusion, the wind effect and density-related terms. They also take into account the internal hydrostatic waves. They appear between two layers of water with different densities. They are not as fast

as the external gravity waves. The characteristic timescale of these terms is defined as

$$\Delta t \propto \max\left(\frac{\Delta xy^2}{\nu_h}, \frac{\Delta xy}{\|\mathbf{u}\| + \sqrt{gH\rho'/\rho}}\right)$$

Finally, the missing term, the Coriolis force, with $\Delta t \propto \frac{1}{f}$, is treated semi-implicitly. This decision is due to the necessity for a centered temporal scheme to ensure that the Coriolis force vector, perpendicular to velocity, neither generates nor dissipates kinetic energy. The model dealing with semi-implicit terms is centered, hence justifying the inclusion of the Coriolis term among these semi-implicit terms. This does not significantly increase the computational cost as the Coriolis force is a linear source term.

2.2. Two equations turbulence closure model

The turbulence closure model known as the Generic Length Scale (GLS) by Umlauf and Burchard (2003) solves a pair of equations governing the turbulent kinetic energy (TKE), denoted k, and the auxiliary turbulent variable, represented by Ψ. These are advection-diffusion equations with source terms. Both k and Ψ are positive fields that obey:

$$\frac{\partial k}{\partial t} + \boldsymbol{\nabla}_h \cdot (\mathbf{u}k) + \frac{\partial (wk)}{\partial z} = \boldsymbol{\nabla}_h \cdot (\nu_h \boldsymbol{\nabla}_h k) + \frac{\partial}{\partial z}\left(\frac{\nu_v}{\sigma_k}\frac{\partial k}{\partial z}\right) + P - \epsilon + B$$
$$\frac{\partial \Psi}{\partial t} + \boldsymbol{\nabla}_h \cdot (\mathbf{u}\Psi) + \frac{\partial (w\Psi)}{\partial z} = \boldsymbol{\nabla}_h \cdot (\nu_h \boldsymbol{\nabla}_h \Psi) + \frac{\partial}{\partial z}\left(\frac{\nu_v}{\sigma_\Psi}\frac{\partial \Psi}{\partial z}\right) + \frac{\Psi}{k}(c_1 P - c_2\epsilon + c_3 B)$$

where σ_k and σ_Ψ are the Schmidt numbers for k and Ψ respectively. c_1, c_2, c_3 are constants determined by the model.

Contrary to the Zero-equation parametrizations such as Pacanowski and Philander (Pacanowski and Philander, 1981) or the K-profil Parametrization (Large et al., 1994; Roekel et al., 2018) that parametrize the eddy viscosity as a function of the mean flow state, these equations take into account prognostic turbulent variables. P is the production term of TKE and buoyancy while ϵ is the dissipation rate of TKE. B is a production or destruction term depending on the stratification. P and B are defined as

$$P = \nu_v \left(\left(\frac{\partial u}{\partial z}\right)^2 + \left(\frac{\partial v}{\partial z}\right)^2\right) \tag{7}$$
$$B = \kappa_v \frac{g}{\rho_0}\frac{\partial \rho}{\partial z} \tag{8}$$

The term P consistently holds a semi-positive value, indicating that horizontal velocity shear generates turbulence. P converts kinetic energy of the mean flow into turbulent kinetic energy. On the contrary, the sign of B can fluctuate: under stable stratification, where $\frac{\partial \rho}{\partial z} < 0$, or in simpler terms, denser water is positioned below lighter water, B adopts a negative value, converting turbulent kinetic energy into gravitational potential energy. Consequently, this stratification tends to inhibit turbulence. In the case of unstable stratification, B becomes positive, transforming potential energy into turbulence. Burchard (2002) emphasized that the numerical implementation of B and P should maintain energy conservation, ensuring that the increase in TKE caused by P aligns with the corresponding loss of kinetic energy of the mean flow. Additionally, the dissipation term, ϵ, is always positive and refers to the dissipation of TKE into heat mainly at the smallest scale of motion.

Concerning Ψ, the source terms are dependent of P, B and ϵ. But they are scaled by Ψ/k and the empirical constants c_1, c_2 and c_3. The meaning and the unity of the variable Ψ are not straightforward.

For instance, $p = -1$, $m = 1/2$ and $n = -1$ gives the $k - \omega$ model (Wilcox, 1988, 2008). In this model, Ψ represent the specific dissipation rate as it is proportional to ϵ/k. It is also known as the turbulence

frequency ω as its units are in s^{-1}. The source terms are multiplied by ϵ/k^2 up to a coefficent.

When $p = 0$, $m = 1$ and $n = 1$, this is the $k - kl$ model from Mellor and Yamada (1982). In this case, Ψ is the product between the turbulent energy and the turbulent length scale. In this closure, the production and destruction terms are scaled by the turbulent length scale.

Finally, in the popular $k - \epsilon$ model, where $p = 3$, $m = 3/2$ and $n = -1$, Ψ is the TKE dissipation rate. This means that the source terms are multiplied by the ratio of the TKE dissipation rate and the TKE.

In numerous ocean models, the horizontal advection of k and Ψ is disregarded, assuming relatively long transport timescales. In addition, the vertical advection is disregarded, considering dimensional analysis on the continuity equation. The same applies to the horizontal diffusion.

The two equations become

$$\frac{\partial k}{\partial t} = \frac{\partial}{\partial z}\left(\frac{\nu_v}{\sigma_k}\frac{\partial k}{\partial z}\right) + P + B - \epsilon \tag{9}$$

$$\frac{\partial \Psi}{\partial t} = \frac{\partial}{\partial z}\left(\frac{\nu_v}{\sigma_\Psi}\frac{\partial \Psi}{\partial z}\right) + \frac{\Psi}{k}\left(c_1 P + c_3 B - C_2 \epsilon\right) \tag{10}$$

The TKE dissipation rate, ϵ, is computed using the following equation:

$$\epsilon = c_0^{3+p/n}\,\frac{k^{3/2+m/n}}{\Psi^{1/n}} \tag{11}$$

where c_0, m, n, p are constants. The values of these constants are also given by the model.

Finally, the vertical eddy viscosity and diffusivity, ν_v and κ_v, are computed using the following equation:

$$\nu_v = \frac{c_\nu}{c_0^{3+p/n}} k^{1/2-m/n} \Psi^{1/n} \tag{12}$$

$$\kappa_v = \frac{c_\kappa}{c_0^{3+p/n}} k^{1/2-m/n} \Psi^{1/n} \tag{13}$$

where c_ν and c_κ are non-dimensional stability functions that depend on the vertical gradient of the water velocity and density.

As there are no horizontal flux terms, there is no need for boundary conditions on the lateral boundaries. Regarding the boundaries at the surface and bottom of the domain, they are determined by the wall conditions. The boundaries flux for k are 0 while the Neumann conditions on Ψ are

$$\frac{\nu_v}{\sigma_\Psi}\frac{\partial \Psi}{\partial z} = -n\frac{\nu_v}{\sigma_\Psi} c_0^p k^m \kappa^n \left(\frac{\Delta z}{2} + z_{0,s}\right)^{n-1} \qquad \mathbf{x} \in \Gamma_s \tag{14a}$$

$$\frac{\nu_v}{\sigma_\Psi}\frac{\partial \Psi}{\partial z} = \quad n\frac{\nu_v}{\sigma_\Psi} c_0^p k^m \kappa^n \left(\frac{\Delta z}{2} + z_{0,b}\right)^{n-1} \qquad \mathbf{x} \in \Gamma_b \tag{14b}$$

where $z_{0,s}$ and $z_{0,b}$ are the roughness length scales at the surface and bottom respectively. Δz is the vertical grid size. As the gradients cannot be computated right at the surface and bottom because Ψ can change rapidly. Therefore, the gradients are computed at the middle of the first and last vertical layers.

3. Temporal scheme

The aim of this section is to propose suitable time discretizations that efficiently resolve multiscale behaviour of a stiff problem. Several methodologies exist for integrating systems of ordinary differential equations, which encompass multistep approaches dealing with the system in fully explicit, fully implicit, or split implicit–explicit manners. This study specifically explores the utilization of second-order split IMEX integrators. These temporal integrators partition the hydrodynamic equation's right-hand side into three

components: an explicit fast yet less computationally intensive part, an explicit non-stiff part and a semi-implicit stiff part with a smaller timescale than the previous one. To exemplify, let us consider the subsequent ordinary differential equation:

$$\frac{\mathrm{d}y}{\mathrm{d}t} = f^{\mathrm{xy}}(y) + f^{\mathrm{z}}(y) + F^{\mathrm{fast}}(y), \quad t \in (0, T) \tag{15}$$

with the initial value $y(0) = y_0$. The notation $f^{\mathrm{xy}}(y)$ represents the slow horizontal processes integrated explicitly, while $f^{\mathrm{z}}(y)$ denotes the vertical terms treated semi-implicitly. $F^{\mathrm{fast}}(y)$ symbolizes the 2D dynamics characterized by a short timescale.

The semi-implicit term needs to be further developed as it may contain non-linear operators. Resolving non-linear semi-implicit terms requires the use of non-linear solvers such as the ones based on the Newton-Raphson method. However, employing such solvers can significantly increase computational time. To address this issue, the semi-implicit terms are divided into linear and non-linear components. The non-linear portion is addressed as a product between an explicit coefficient and an implicit one, while the linear part is treated completly semi-implicitly. This approach allows for handling semi-implicit terms without a substantial increase in computational time. The previous equation becomes :

$$\frac{\mathrm{d}y}{\mathrm{d}t} = f^{\mathrm{xy}}(y) + f^{\mathrm{z0}}(y) + f^{\mathrm{z1}}(y)\, y + F^{\mathrm{fast}}(y), \quad t \in (0, T) \tag{16}$$

where $f^{\mathrm{z0}}(y)$ and $f^{\mathrm{z1}}(y)\, y$ are the linear and non-linear components of the semi-implicit term respectively.

The fundamental idea behind the method presented in this paper is to employ a split-time scheme composed of Runge-Kutta methods. These Runge-Kutta methods use two different time steps: Δt for the 3D evolving terms and $\Delta T = \frac{\Delta t}{M}$ for the fast terms, where M represents the largest integer close to the ratio of characteristic speeds. As the primary aim of this paper is to developed a second-order global scheme, the selection of these Runge-Kutta methods cannot be arbitrary.

3.1. Choice of the Runge-Kutta schemes

The choice of the temporal discretization methods involves several constraints. Depending on the equations, they can vary.

3.1.1. Hydrodynamic equations

For the hydrodynamic equations, the discontinuous Galerkin finite element method, when dealing with an advection problem, has eigenvalues along the imaginary axis. Due to diffusion terms, these eigenvalues are slightly shifted towards the left. In other words, they are not purely imaginary but remain very close to the axis. Therefore, when employing a temporal method of order one, an extremely small time step is required. Hence, the choice of a temporal scheme of order two is made. In aiming for a second-order scheme over the final time step, each term within the ordinary differential equation must be treated using, at minimum, a second-order method. In other words, it is imperative to identify an order two explicit Runge-Kutta method for the explicit terms along with a semi-implicit second-order Runge-Kutta for the linear semi-implicit stiff term. Moreover, a Runge-Kutta method capable of integrating a term comprising a product of functions, one handled explicitly and the other semi-implicitly, is necessary. One first easy direct choice is to use the same explicit RK for the fast term as the one used for the explicit slow terms.

By doing this choice, this gives the following split IMEX Runge-Kutta method for the 3D terms:

$$
\begin{aligned}
y_{n+i} &= y_n + \alpha_{00}\Delta t f^{\mathrm{xy}}(y_n) \\
&\quad + \beta_{00}\Delta t f^{\mathrm{z0}}(y_{n+i}) \\
&\quad + \gamma_{00}\Delta f^{\mathrm{z1}}(y_n)\; y_{n+i} \qquad (17) \\
y_{n+1} &= y_n + \alpha_{10}\Delta t f^{\mathrm{xy}}(y_n) + \alpha_{11}\Delta t f^{\mathrm{xy}}(y_{n+i}) \\
&\quad + \beta_{10}\Delta t f^{\mathrm{z0}}(y_{n+i}) + \beta_{11}\Delta t f^{\mathrm{z0}}(y_{n+1}) \\
&\quad + \gamma_{10}\Delta f^{\mathrm{z1}}(y_n)\; y_{n+i} + \gamma_{11}\Delta f^{\mathrm{z1}}(y_n)\; y_{n+1} \\
&\quad + \gamma_{12}\Delta f^{\mathrm{z1}}(y_{n+i})\; y_{n+i} + \gamma_{13}\Delta f^{\mathrm{z1}}(y_{n+i})\; y_{n+1} \qquad (18)
\end{aligned}
$$

This constitutes the expression of the complete temporal scheme without constraints with its partial stage length arbitrary. Essentially, it forms a system with 12 unknowns: one coefficient representing the temporal position achieved at the end of the first sub-time step and eleven coefficients multiplying the slopes, or in other words, the derivatives in the form of α_{mn}, β_{mn} and γ_{mn}. The α_{mn} coefficients correspond to the explicit slow terms, while the β_{mn} coefficients are related to the semi-implicit stiff terms. Finally, the γ_{mn} coefficients are associated with the explicit-implicit cross terms. The indices m and n represent the stage number and the term number respectively. The first index m varies from 0 to 1, while the second index n varies from 0 to 1 for the first stage and from 0 to 3 for the second stage.

Additionally, in this model, we aim to enforce the final scheme to be low storage, implying the use of only a limited number of temporal values at each stage of the method. This constraint is crucial as it significantly simplifies the method's implementation, particularly because the equations involve Arbitrary Lagrangian-Eulerian formulations. This means that a reduced number of terms need to account for mesh movements. In essence, at each stage, a maximum of three temporal values are present: the value at the beginning of the temporal scheme, the value at the end of the current stage and the value used in the slope to move the variables. For the first stage, it does not change anything. However, for the second stage, this implies that the derivatives can not use simultaniously values at t_n and t_{n+i}. Consequently, this gives two choices. The first is to keep the value at t_n and the value at t_{n+1} in the right-hand side. This gives

$$\alpha_{11} = \beta_{10} = \gamma_{10} = \gamma_{12} = \gamma_{13} = 0$$

In this configuration, the second stage becomes

$$
\begin{aligned}
y_{n+1} &= y_n + \alpha_{10}\Delta t f^{\mathrm{xy}}(y_n) \\
&\quad + \beta_{11}\Delta t f^{\mathrm{z0}}(y_{n+1}) \\
&\quad + \gamma_{11}\Delta t f^{\mathrm{z1}}(y_n)\; y_{n+1}
\end{aligned}
$$

One can see that this scheme is not second-order accurate by construction. Indeed, the value computed at the first stage is not used in the second stage. The right choice is to keep the value at t_{n+i} and at t_{n+1} in the right-hand side. This gives

$$\alpha_{10} = \gamma_{10} = \gamma_{11} = 0$$

The second time loop becomes

$$
\begin{aligned}
y_{n+1} = y_n &+ \alpha_{11}\Delta t f^{\mathrm{xy}}(y_{n+i}) \\
&+ \beta_{10}\Delta t f^{\mathrm{z0}}(y_{n+i}) + \beta_{11}\Delta t f^{\mathrm{z0}}(y_{n+1}) \\
&+ \gamma_{12}\Delta f^{\mathrm{z1}}(y_{n+i})\ y_{n+i} \\
&+ \gamma_{13}\Delta f^{\mathrm{z1}}(y_{n+i})\ y_{n+1}
\end{aligned}
$$

Finally, the last constraint is to ensure that the scheme is second-order accurate. To achieve this, the Taylor series expansion of y_{n+1} must match the result of the temporal scheme up to order 2. The only way to do so is the take following split IMEX Runge-Kutta method for the slow and stiff terms:

$$
\begin{aligned}
y_{n+\frac{1}{2}} = y_n &+ \frac{1}{2}\Delta t f^{\mathrm{xy}}(y_n) \\
&+ \frac{1}{2}\Delta t f^{\mathrm{z0}}(y_{n+\frac{1}{2}}) \\
&+ \frac{1}{2}\Delta f^{\mathrm{z1}}(y_n)\ y_{n+\frac{1}{2}} \\
y_{n+1} = y_n &+ \Delta t f^{\mathrm{xy}}(y_{n+\frac{1}{2}}) \\
&+ \Delta t f^{\mathrm{z0}}(y_{n+\frac{1}{2}}) \\
&+ \Delta f^{\mathrm{z1}}(y_{n+\frac{1}{2}})\ y_{n+\frac{1}{2}}
\end{aligned}
\tag{19}
$$

The demonstration of the order of this scheme is done Section 3.3. Concerning the fast terms, they are computed with the same explicit Runge-Kutta method as the slow explicit terms. This gives

$$
\begin{aligned}
y_{n+\frac{1}{2}} &= y_n + \frac{1}{2}\Delta T F^{\mathrm{fast}}(y_n) \\
y_{n+1} &= y_n + \Delta T F^{\mathrm{fast}}(y_{n+\frac{1}{2}})
\end{aligned}
\tag{20}
$$

3.1.2. Two equations turbulence closure model

As for the turbulence closure equations, a second-order temporal scheme is also desirable to keep the global scheme of order 2. The aim is to use vertical viscosity and diffusivity value that are calculated at time $n + \frac{1}{2}$ in the diffusion terms of the hydrodynamic equations. To satisfy both constraints, the simplest choice is to employ the same temporal scheme as that described in the preceding section.

However, this is not sufficient. An additional requirement for these equations is that the scheme must be positive. This means that if a simulation starts with positive field values, they must remain positive throughout all the simulation regardless of the hydrodynamics.

Positive production terms pose no issues. The diffusion term in these equations also doesn't raise any concerns. The stability of the Runge-Kutta as well as the Finite-Volume methods guaranties the positivity of the variables under the diffusion. The only problematic terms is the destruction terms. The aim is to avoid situations where, within a time step, more is destroyed than what is produced and received by diffusion. This would result in a negative value for k or Ψ, which is not physically possible. Moreover, this can lead to negative viscosity or diffusivity coefficients. To avoid this, an appropriate approach involves using Patankar techniques (Patankar, 1980) on the destruction terms. As shown by Burchard et al. (2003), Patankar methods are employed to ensure the positivity of turbulent variables. Isgin and Ranocha (2023) demonstrated the way to implement these techniques in a temporal scheme of order two. For the sake of brevity, the details of the demonstration of the order are not given here again.

The diffusion term and the positive production terms follow the temporal scheme presented before. The

temporal scheme for destruction terms is the following:

$$
\begin{aligned}
y_{n+\frac{1}{2}} &= y_n + \frac{\Delta T}{2} D(y_n) \frac{y_{n+\frac{1}{2}}}{y_n} \\
y_{n+1} &= y_n + \Delta T D(y_{n+\frac{1}{2}}) \frac{y_{n+1}\, y_n}{\left(y_{n+\frac{1}{2}}\right)^2}
\end{aligned}
\tag{21}
$$

where $D(y)$ is the negative destruction term.

3.2. Split IMEX Runge-Kutta method

In order to obtain the final scheme, one needs to combine the explicit and implicit Runge-Kutta methods for the 3D terms with the explicit Runge-Kutta method for the fast 2D terms. Coupling the fast terms with the slow explicit terms has already be done in Ishimwe et al. (2023). In the context of this model, coupling between stiff and fast terms proves to be notably intricate.

For the first sub iteration, the implicit aspect of this scheme anticipates computing the value of the variable $y_{n+\frac{1}{2}}$ for each iteration within the temporal loop of the fast scheme. However, this contradicts the core purpose of splitting. The aim is to compute the 3D terms a fixed number of times independent of the number of fast time steps. This requires taking inspiration from predictor-corrector methods to handle the connection between the implicit elements.

The description of the first sub-time step of the 3D component follows. Initially, before entering the temporal loop of the fast terms, the contribution of the slow adn stiff terms must be calculated. During the evaluation of the slow explicit terms, a prediction of the implicit vertical terms is also computed. This prediction estimates the value of the implicit slope without considering the fast terms. Using this slope alongside the contribution from the explicit slow derivative advances the fast terms with a smaller time step. Following multiple Runge-Kutta iterations, the contributions of all fast slopes can be computed. By using these fast slopes along with the explicit slow slopes, the unknown variable's value can be calculated, this time incorporating the correct value for the implicit slope. Consequently, this yields the value of y at the midpoint of the time step.

Regarding the second sub-time step, upon close examination of the Runge-Kutta equations described in the preceding section, it is noticeable that the semi-implicit functions are no longer computed using the future value of y but rather utilizing the midpoint value. This implies that the second time step is entirely explicit. Consequently, the coupling between the slow, the stiff and the fast terms becomes more straightforward and is directly inspired by Ishimwe et al. (2023). This implies that all 3D terms are computed before the temporal loops of the fast terms and then the entirety advances during the fast Runge-Kutta iterations.

The complete scheme is presented as follows:

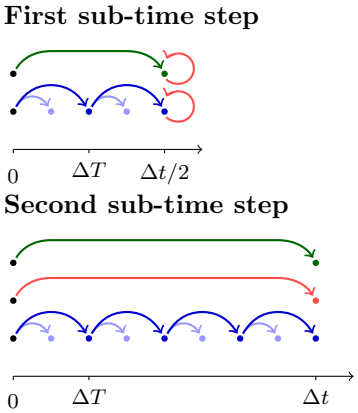

Figure 1: Split IMEX scheme composed of two RK2 and one IRK2. In the first sub-time step, the green arrows represents $f^{\text{xy}}(y_n)$, the first and second red arrows are $f^{\text{z0}}(y^*) + f^{\text{z1}}(y_n)\, y^*$ and $f^{\text{z0}}(y_{n+\frac{1}{2}}) + f^{\text{z1}}(y_n)\, y_{n+\frac{1}{2}}$ respectively. The blue arrows represent the computation of each $f^{\text{fast}}(y)$. In the second sub-time step, the green arrows represents $f^{\text{xy}}(y_{n+\frac{1}{2}})$ while the red arrow is $f^{\text{z0}}(y_{n+\frac{1}{2}}) + f^{\text{z1}}(y_{n+\frac{1}{2}})\, y_{n+\frac{1}{2}}$.

First sub-time step

$$y_* = y_n + \frac{1}{2}\Delta t \left(f^{\text{xy}}(y_n) + f^{\text{z0}}(y_*) + f^{\text{z1}}(y_n)\, y_*\right)$$

$$F^{\text{fast}} = 0$$

$$\text{for } j = 0, \dots, \frac{M}{2} - 1$$

$$y_{n+\frac{j+1/2}{M}} = y_{n+\frac{j}{M}} + \frac{1}{2}\Delta T \left(F^{\text{fast}}(y_{n+\frac{j+1}{M}}) + f^{\text{xy}}(y_n) + f^{\text{z0}}(y_*) + f^{\text{z1}}(y_n)\, y_*\right)$$

$$y_{n+\frac{j+1}{M}} = y_{n+\frac{j}{M}} + \Delta T \left(F^{\text{fast}}(y_{n+\frac{j+1/2}{M}}) + f^{\text{xy}}(y_*) + f^{\text{z0}}(y_*) + f^{\text{z1}}(y_*)\, y_*\right)$$

$$F^{\text{fast}} = F^{\text{fast}} + F^{\text{fast}}(y_{n+\frac{j+1/2}{M}})$$

$$y_{n+\frac{1}{2}} = y_n + \frac{1}{2}\Delta t \left(f^{\text{xy}}(y_n) + f^{\text{z0}}(y_{n+\frac{1}{2}}) + f^{\text{z1}}(y_n)\, y_{n+\frac{1}{2}} + F^{\text{fast}}\right)$$

Second sub-time step

$$F^{\text{fast}} = 0$$

$$\text{for } j = 0, \dots, M - 1$$

$$y_{n+\frac{j+1/2}{M}} = y_{n+\frac{j}{M}} + \frac{1}{2}\Delta T \left(F^{\text{fast}}(y_{n+\frac{j+1}{M}}) + f^{\text{xy}}(y_n) + f^{\text{z0}}(y_{n+\frac{1}{2}}) + f^{\text{z1}}(y_n)\, y_{n+\frac{1}{2}}\right)$$

$$y_{n+\frac{j+1}{M}} = y_{n+\frac{j}{M}} + \Delta T \left(F^{\text{fast}}(y_{n+\frac{j+1/2}{M}}) + f^{\text{xy}}(y_{n+\frac{1}{2}}) + f^{\text{z0}}(y_{n+\frac{1}{2}}) + f^{\text{z1}}(y_{n+\frac{1}{2}})\, y_{n+\frac{1}{2}}\right)$$

$$F^{\text{fast}} = F^{\text{fast}} + F^{\text{fast}}(y_{n+\frac{j+1/2}{M}})$$

$$y_{n+1} = y_n + \Delta t \left(f^{\text{xy}}(y_{n+\frac{1}{2}}) + f^{\text{z0}}(y_{n+\frac{1}{2}}) + f^{\text{z1}}(y_{n+\frac{1}{2}})\, y_{n+\frac{1}{2}} + F^{\text{fast}}\right)$$

The whole process is summarised in the Figure 1 and the Algorithm 1. While this temporal method uses two established RK methods, the resultant splitting mechanism is novel and unique.

Algorithm 1: split IMEX scheme of order 2

Data: Model state variable y_n, $m = M/2$

First sub-time step

$\mathrm{f}^{\mathrm{xy}} \leftarrow f^{\mathrm{xy}}(y_n)$

$\mathrm{f}^{\mathrm{z1}} \leftarrow f^{\mathrm{z1}}(y_n)$

$y^* \leftarrow y_n + \frac{\Delta t}{2}(\mathrm{f}^{\mathrm{xy}} + f^{\mathrm{z0}}(y^*) + \mathrm{f}^{\mathrm{z1}}\ y^*)$

$\mathrm{f}^{\mathrm{z0}} \leftarrow f^{\mathrm{z0}}(y^*)$

$y \leftarrow y_n$

$F^{\mathrm{fast}} \leftarrow \mathbf{0}$

for $j = 1, \ldots, M/2$ **do**

  $\mathrm{f}^{\mathrm{fast}} \leftarrow f^{\mathrm{fast}}(y)$

  $\mathrm{f}^{\mathrm{fast}} \leftarrow f^{\mathrm{fast}}(y + \frac{1}{2}\Delta T(\mathrm{f}^{\mathrm{fast}} + \mathrm{f}^{\mathrm{xy}} + \mathrm{f}^{\mathrm{z0}} + \mathrm{f}^{\mathrm{z1}}\ y^*))$

  $y \leftarrow y + \Delta T(\mathrm{f}^{\mathrm{fast}} + \mathrm{f}^{\mathrm{xy}} + \mathrm{f}^{\mathrm{z0}} + \mathrm{f}^{\mathrm{z1}}\ y^*)$

  $F^{\mathrm{fast}} \leftarrow F^{\mathrm{fast}} + \Delta T \mathrm{f}^{\mathrm{fast}}$

$y_{n+\frac{1}{2}} \leftarrow y_n + \frac{\Delta t}{2}(\mathrm{f}^{\mathrm{xy}} + f^{\mathrm{z0}}(y_{n+\frac{1}{2}}) + \mathrm{f}^{\mathrm{z1}}\ y_{n+\frac{1}{2}}) + F^{\mathrm{fast}}$

Second sub-time step

$\mathrm{f}^{\mathrm{xy}} \leftarrow f^{\mathrm{xy}}(y_{n+\frac{1}{2}})$

$\mathrm{f}^{\mathrm{z0}} \leftarrow f^{\mathrm{z0}}(y_{n+\frac{1}{2}})$

$\mathrm{f}^{\mathrm{z1}} \leftarrow f^{\mathrm{z1}}(y_{n+\frac{1}{2}})$

$F^{\mathrm{fast}} \leftarrow \mathbf{0}$

for $j = 1, \ldots, M$ **do**

  $\mathrm{f}^{\mathrm{fast}} \leftarrow f^{\mathrm{fast}}(y)$

  $\mathrm{f}^{\mathrm{fast}} \leftarrow f^{\mathrm{fast}}(y + \frac{1}{2}\Delta T(\mathrm{f}^{\mathrm{fast}} + \mathrm{f}^{\mathrm{xy}} + \mathrm{f}^{\mathrm{z0}} + \mathrm{f}^{\mathrm{z1}}\ y_{n+\frac{1}{2}}))$

  $y \leftarrow y + \Delta T(\mathrm{f}^{\mathrm{fast}} + \mathrm{f}^{\mathrm{xy}} + \mathrm{f}^{\mathrm{z0}} + \mathrm{f}^{\mathrm{z1}}\ y_{n+\frac{1}{2}})$

  $F^{\mathrm{fast}} \leftarrow F^{\mathrm{fast}} + \Delta T \mathrm{f}^{\mathrm{fast}}$

$y_{n+1} \leftarrow y_n + \Delta t \left(\mathrm{f}^{\mathrm{xy}} + \mathrm{f}^{\mathrm{z0}} + \mathrm{f}^{\mathrm{z1}}\ y_{n+\frac{1}{2}}\right) + F^{\mathrm{fast}}$

3.3. Order of precision

The order of the scheme is obtained by comparing the Taylor series expansion of the scheme with the Taylor series expansion of the solution of the ODE. The order of the scheme is the highest order of the same terms between them. The expression of the Taylor series y_{n+1} is given by

$$\begin{aligned} y_{n+1} =& y_n + \Delta t y_n^{'} + \frac{\Delta t^2}{2} y_n^{''} + O(\Delta t^3) \\ =& y_n + \Delta t \left(f_n^{xy} + f_n^{z0} + f_n^{z1}\, y_n + F_n \right) \\ &+ \frac{\Delta t^2}{2} \left(\left(f_n^{xy} + f_n^{z0} + f_n^{z1}\, y_n + F_n \right)^{'} \left(f_n^{xy} + f_n^{z0} + f_n^{z1}\, y_n + F_n \right) \right) \\ &+ O(\Delta t^3) \end{aligned} \tag{22}$$

with $f_n^{xy} = f^{\mathrm{xy}}(y_n)$, $f_n^{z0} = f^{\mathrm{z0}}(y_n)$, $f_n^{z1} = f^{\mathrm{z1}}(y_n)$ and $F_n = F^{\mathrm{fast}}(y_n)$.

A conventional Runge-Kutta order analysis involves calculating each iteration of the slopes and adding them to derive the final expression for y_{n+1}. However, in a split temporal scheme, showcasing the outcome of each 2D sub-step is not practical due to the multitude of terms involved. Therefore, for clarity, only the assessments of y at the 3D sub-steps, encompassing $y_{n+\frac{1}{2}}$ and y_{n+1}, are computed instead. However, rest assured that the comprehensive details of the small time-step 2D loops have been provided in the article Ishimwe et al. (2023). The result of a whole fast Runge-Kutta iteration has also been expressed. For a given k^{slow} and M, the result of the fast Runge-Kutta iteration is

$$\begin{aligned} y_M =& y_n + M\Delta T \left(F_n + k^{\mathrm{slow}} \right) + \frac{M^2 \Delta T^2}{2} \left(F_n + k^{\mathrm{slow}} \right) F_n^{'} + O(M^3 \Delta T^3) \\ =& y_n + \Delta t \left(F_n + k^{\mathrm{slow}} \right) + \frac{\Delta t^2}{2} \left(F_n + k^{\mathrm{slow}} \right) F_n^{'} + O(\Delta t^3) \end{aligned}$$

This result is denoted $RK2(k^{\mathrm{slow}}, M)$. To determine the order of accuracy of the global method, the split IMEX RK2 method is unrolled. The two sub-steps are computed separately because the first sub-step is implicit, while the second sub-step is explicit. Moreover, the prediction of the implicit terms is analysed separately from the correction. In the first sub steps, the predicted 3D slope is denoted $k_1^{*,\mathrm{slow}}$ and the corrected 3D slope is denoted k_1^{slow}. The former ones are computed without considering the fast terms while the latter ones are computed with the fast terms. The predicted slope is given by

$$\begin{aligned} k_1^{*,\mathrm{slow}} =& f_n^{xy} + f_n^{*,z0} + f_n^{z1}\, y_n^* \\ =& f_n^{xy} + f_n^{z0} + f_n^{z1}\, y_n \\ &+ \frac{\Delta t}{2} \left(f_n^{xy} + f_n^{z0} + f_n^{z1}\, y_n \right) f_n^{i'} \\ &+ \frac{\Delta t}{2} f_n^{z1} \left(f_n^{xy} + f_n^{z0} + f_n^{z1}\, y_n \right) \\ &+ O(\Delta t^2) \end{aligned}$$

Following Algorithm 1, the value of RK2$(k_1^{*,\mathrm{slow}}, \frac{M}{2})$ can be obtained. Consequently, the sum of the fast slopes can be computed. This sum is denoted F_1^{fast} and is given by

$$F_1^{\mathrm{fast}} = \frac{\Delta t}{2} F_n + \frac{1}{2} \left(\frac{\Delta t}{2} \right)^2 F_n F_n^{'} + O(\Delta t^3)$$

The value of $y_{n+\frac{1}{2}}$ can now be expressed as

$$\begin{aligned} y_{n+\frac{1}{2}} =& y_n + \frac{\Delta t}{2}\left(f_n^{xy} + f_n^{z0} + f_n^{z1}\, y_n + F_n\right) \\ &+ \frac{\Delta t^2}{8}\left(f_n^{xy} + f_n^{z0} + f_n^{z1}\, y_n + F_n\right) F_n^{'} \\ &+ \frac{\Delta t^2}{4}\left(f_n^{xy} + f_n^{z0} + f_n^{z1}\, y_n + F_n\right) f_n^{i'} \\ &+ \frac{\Delta t^2}{4} f_n^{z1}\left(f_n^{xy} + f_n^{z0} + f_n^{z1}\, y_n + F_n\right) \\ &+ O(\Delta t^3) \end{aligned} \tag{23}$$

The second sub step computes explicitely the slow, the stiff and the fast terms. The slope denoted k_2^{slow} is

$$\begin{aligned} k_2^{\text{slow}} =& f^{\text{xy}}(y_{n+\frac{1}{2}}) + f^{\text{z0}}(y_{n+\frac{1}{2}}) + f^{\text{z1}}(y_{n+\frac{1}{2}})\, y_{n+\frac{1}{2}} \\ =& f_n^{xy} + f_n^{z0} + f_n^{z1}\, y_n \\ &+ \frac{\Delta t}{2}\left(f_n^{xy} + f_n^{z0} + f_n^{z1}\, y_n + F_n\right)\left(f_n^{xy} + f_n^{z0} + f_n^{z1}\, y_n\right)^{'} \\ &+ O(\Delta t^2) \end{aligned}$$

The final value of y_{n+1} is given by RK2(k_2^{slow},M).

$$\begin{aligned} y_{n+1} =& y_n + \Delta t\left(f_n^{xy} + f_n^{z0} + f_n^{z1}\, y_n + F_n\right) \\ &+ \frac{\Delta t^2}{2}\left(f_n^{xy} + f_n^{z0} + f_n^{z1}\, y_n + F_n\right)\left(f_n^{xy} + f_n^{z0} + f_n^{z1}\, y_n + F_n\right)^{'} \\ &+ O(\Delta t^3) \end{aligned} \tag{24}$$

Comparing the Taylor series expansion of y_{n+1} (Equation 24) with the Taylor series expansion of the solution of the ODE (Equation 22), one can see that the order of the scheme is 2.

As stated before, the Patankar modified scheme is also of order 2. This is mentionned by Isgin and Ranocha (2023). The demonstration is done in Kopecz and Meister (2018).

3.4. Stability region

The stability region of a numerical scheme is the set of complex numbers z such that the numerical scheme applied to the linear ODE is stable.

3.4.1. Stability of the IMEX Runge-Kutta method

In the case of the split IMEX RK2 scheme, there are three different characteristic speeds. Therefore, this configuration should be taken into account. The linear ODE becomes

$$\frac{\partial y}{\partial t} = \lambda_{xy} y + \lambda_z y + \Lambda y$$

with respectively λ_{xy}, λ_z and Λ the complex coefficient of the linear function of the horizontal explicit terms, the vertical semi-implicit terms and the fast terms.

The amplification factor of the scheme is defined as the ratio between the value of y at the end of the time step and the value at the beginning of the time step. The result of the fast Runge-Kutta iterations,

denoted $RK2(k^{\text{slow}}, M)$, is

$$y_M = y_n A^M + k^{\text{slow}} \left(\Delta T + \Lambda \frac{\Delta T^2}{2} \right) \frac{1 - A^M}{1 - A}$$

with $A = 1 + \Lambda \Delta T + \Lambda^2 \frac{\Delta T^2}{2}$ and $\Lambda \neq 0$, $\Delta T \neq 0$.

Once again, the analysis of the complete temporal scheme is divided into two due to the specific configuration of this IMEX scheme. Indeed, the implicit aspect of the first sub-time step, coupled with its predictor-corrector nature, complicates the analysis. The value resulting from the prediction offers a insight into the scheme's treatment concerning the 3D terms and impacts the overall stability of the scheme.

The predicted value is

$$y^* = y_n \frac{1 + \frac{\Delta t}{2} \lambda_{xy}}{1 - \frac{\Delta t}{2} \lambda_z}$$

The corresponding slope is

$$\begin{aligned} k_1^{*,\text{slow}} &= \lambda_{xy} y_n + \lambda_z y^* \\ &= y_n \left(\lambda_{xy} + \lambda_z \frac{1 + \frac{\Delta t}{2} \lambda_{xy}}{1 - \frac{\Delta t}{2} \lambda_z} \right) \end{aligned}$$

The predicted value is then used to compute the fast Runge-Kutta iterations. The result of the fast iterations gives

$$\begin{aligned} y^*_{n+\frac{1}{2}} =& RK2(k_1^{*,\text{slow}}, \frac{M}{2}) \\ =& y_n A^{\frac{M}{2}} \\ &+ y_n \left(\lambda_{xy} + \lambda_z \frac{1 + \frac{\Delta t}{2} \lambda_{xy}}{1 - \frac{\Delta t}{2} \lambda_z} \right) \left(\Delta T + \Lambda \frac{\Delta T^2}{2} \right) \frac{1 - A^{\frac{M}{2}}}{1 - A} \end{aligned}$$

As Algorithm 1 shows, this value is only a prediction to obtained the fast slopes. They are combined with the slow explicit slope to obtain the final value using the correction of the implicit term. This gives the following expression

$$\begin{aligned} y_{n+\frac{1}{2}} &= y_n A^{\frac{M}{2}} + \lambda_{xy} y_n \left(\Delta T + \Lambda \frac{\Delta T^2}{2} \right) \frac{1 - A^{\frac{M}{2}}}{1 - A} + \frac{\Delta t}{2} \lambda_z y_{n+\frac{1}{2}} \\ &= y_n \left(\frac{1}{1 - \lambda_z \frac{\Delta t}{2}} \right) \left(\lambda_{xy} \left(\Delta T + \Lambda \frac{\Delta T^2}{2} \right) \frac{1 - A^{\frac{M}{2}}}{1 - A} + A^{\frac{M}{2}} \right) \end{aligned}$$

Using this value, the slope of the second sub-time step, k_2^{slow}, can be computed.

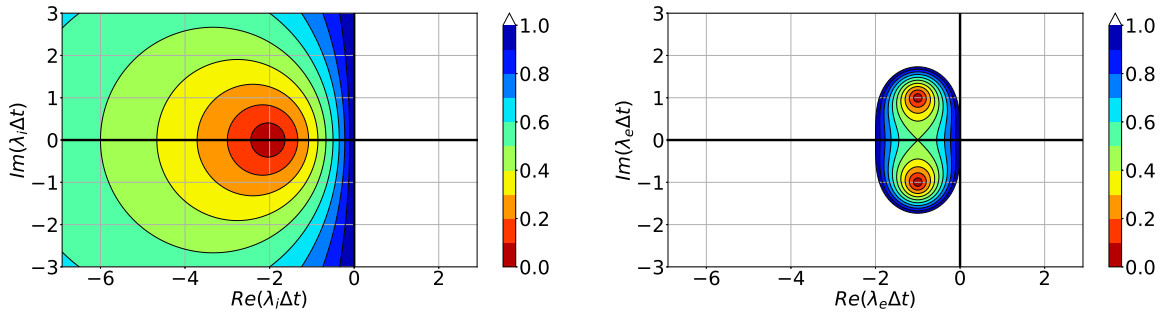

Figure 2: Stability region with only one function with M = 1. The abscissa is the Real part while the ordinates is the Imaginary part of respectively $\lambda_z \Delta t$ and $\lambda_{xy} \Delta t$. The bold lines are the origins.

$$
\begin{aligned}
k_2^{\text{slow}} &= \lambda_{xy} y_{n+\frac{1}{2}} + \lambda_z y_{n+\frac{1}{2}} \\
&= y_n \left(\lambda_{xy} + \lambda_z\right) \left(\frac{1}{1 - \lambda_z \frac{\Delta t}{2}}\right) \left(\lambda_{xy} \left(\Delta T + \Lambda \frac{\Delta T^2}{2}\right) \frac{1 - A^{\frac{M}{2}}}{1 - A} + A^{\frac{M}{2}}\right)
\end{aligned}
$$

Consequently, the value of y_{n+1} can be expressed as

$$
\begin{aligned}
y_{n+1} =& RK2(k_2^{\text{slow}}, M) \\
=& y_n A^M \\
&+ y_n \left(\frac{\lambda_{xy} + \lambda_z}{1 - \lambda_z \frac{\Delta t}{2}}\right) \left(\lambda_{xy} \left(\Delta T + \Lambda \frac{\Delta T^2}{2}\right) \frac{1 - A^{\frac{M}{2}}}{1 - A} + A^{\frac{M}{2}}\right) \\
&\left(\Delta T + \Lambda \frac{\Delta T^2}{2}\right) \frac{1 - A^M}{1 - A}
\end{aligned}
$$

Finally, the amplification factor of the scheme is given by

$$
\begin{aligned}
\frac{y_{n+1}}{y_n} =& A^M + \left(\frac{\lambda_{xy} + \lambda_z}{1 - \lambda_z \frac{\Delta t}{2}}\right) \left(\lambda_{xy} \left(\Delta T + \Lambda \frac{\Delta T^2}{2}\right) \frac{1 - A^{\frac{M}{2}}}{1 - A} + A^{\frac{M}{2}}\right) \\
&\left(\Delta T + \Lambda \frac{\Delta T^2}{2}\right) \frac{1 - A^M}{1 - A}
\end{aligned}
$$

The stability region of the scheme is a function of four parameters: λ_{xy}, λ_z, Λ and M, where the first three are complex and the last is a positive integer. Representing the global stability region proves to be highly intricate, given its 7D nature. To simplify the illustration of the function, let us examine the scenario where either λ_{xy}, λ_z or Λ equals zero and M equals 1. The fast term and the explicit slow term using the same temporal scheme, it is shown once. The stability regions depicted in Figure 2 align with those of the conventional RK2 methods and the Crank-Nicolson. Altering the value of M impacts both graphs: regarding the RK2 for the slow process, the stability region decreases while preserving its original shape; conversely, the semi-implicit process, the region stays unconditionally stable for all the negative values.

3.4.2. Stability of the Patankar Runge-Kutta method

In this section, an analyse of the second-order temporal scheme that incorporates the Patankar method is done for the destruction terms of the turbulence closure equations. This scheme is specifically designed to ensure the positivity of the solution of an equation containing a destruction term. To study its stability zone, the focus is on an ODE where the right-hand side comprises only a destruction term. As a reminder, $D(y)$ is negatively signed and may be a function of y. This results in the following ODE:

$$\frac{\partial y}{\partial t} = D(y)$$

The first step of the Patankar method moves the solution to $t = t + \frac{\Delta t}{2}$. This gives

$$\begin{aligned} y_{n+\frac{1}{2}} &= y_n + \frac{\Delta t}{2} D(y_n) \frac{y_{n+\frac{1}{2}}}{y_n} \\ &= \frac{y_n^2}{y_n - \frac{\Delta t}{2} D(y_n)} \end{aligned}$$

The final step of the Patankar gives

$$\begin{aligned} y_{n+1} &= y_n + \Delta t D(y_{n+\frac{1}{2}}) \frac{y_{n+1} y_n}{y_{n+\frac{1}{2}}} \\ &= \frac{y_n^5}{y_n^4 - \Delta t D\left(y_{n+\frac{1}{2}}\right) y_n \left(y_n - \frac{\Delta t}{2} D(y_n)\right)^2} \end{aligned}$$

This is the solution of the ODE for a generic destruction term. To study the stability of the scheme, the following case is considered

$$D(y) = \lambda_p y$$

with λ_p a complex number and the real part of λ_p negative.

The amplification factor of the scheme is given by

$$\begin{aligned} \frac{y_{n+1}}{y_n} &= \frac{y_n^4}{y_n^4 - \Delta t \lambda_p y_{n+\frac{1}{2}} \left(y_n - \frac{\Delta t}{2} \lambda_p y_n\right)^2} \\ &= \frac{1}{1 - \Delta t \lambda_p + \frac{\Delta t^2}{2} \lambda_p^2} \end{aligned}$$

The stability region is shown in Figure 3. The scheme is unconditionally stable for all the negative values of $Re(\lambda_p)$. This is consistent with the fact that the Patankar method is designed to ensure the positivity of the solution of an equation containing a destruction term. By definition, the latter is always negative. The figure also demonstrates that the stability region of the second-order Patankar scheme is the inverse of the stability region of a classical second-order Runge-Kutta scheme, with a sign change. This means that the region where the amplification factor is less than zero corresponds to the stability region of the Runge-Kutta scheme with a negative sign, whereas it is greater than zero.

3.5. Application to the hydrodynamics equations

The split IMEX RK2 method is applied to the hydrodynamics equations presented in Section 2.1. Regarding spatial discretization, the first-order discontinuous Galerkin finite element method is employed. A

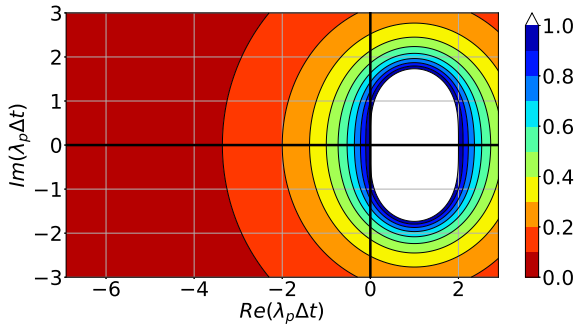

Figure 3: Stability region of the Patankar method. The abscissa is the Real part while the ordinates is the Imaginary part of respectively $\lambda_p \Delta t$. The bold lines are the origins.

comprehensive description of this method was previously detailed in Ishimwe et al. (2023). As the same methodology is used here, it is not be reiterated in this paper.

The temporal method is implemented on these discretized equations. Nonetheless, the finite element method incorporates mass matrices. At time n, M^n represents the global mass matrix. Consequently, in order to employ the split IMEX temporal schemes for our specific problem, it is crucial to consider the evolution of the mass matrix throughout the algorithm.

To accommodate the vertical mesh displacement, an Arbitrary Lagrangian-Eulerian scheme is introduced. As the three-dimensional mesh tracks the free surface movement, solely the vertical coordinates experience temporal changes (e.g., (Clare et al., 2022; Pan et al., 2019)).

While not explicitly demonstrated in this article, it is emphasized that the proposed IMEX scheme still adheres to the properties outlined in the previous work. These include tracer consistency, conservation of water volume and conservation of tracer volume.

A complete iteration of the three-dimensional hydrostatic equations is shown in Algorithm 2.

4. Results

The 3D model is assessed by a set of numerical benchmarks. The correct size of the vortices produced by instabilities in a rotating baroclinic benchmark demonstrates the small amount of numerical dispersion introduced by the discrete model. The second-order accuracy of the scheme is demonstrated by the convergence of the error. Then, the ability of the model to reproduce the dynamics of the overflow mixing and entrainment is also demonstrated.

4.1. Baroclinic eddies

The baroclinic eddies test case, initially introduced in Ilıcak et al. (2012), serves as a pivotal benchmark to assess the model capabilities of generating and accurately representing these eddies while minimizing numerical dissipation through the temporal scheme. It has been previously employed in prior studies such as Petersen et al. (2015). However, it is indispensable to include it in this research as it provides an effective means to test the second-order accuracy and performance of our model in this specific context.

This simulation, representing the Antarctic Circumpolar Current, replicates an unstable sinusoidal front dividing warm and cold water masses, resulting in the development of vortices under the influence of horizontal viscosity. Implemented within a three-dimensional box domain, spanning 500 km in length, 160 km in width and 1000 m in depth, the model incorporates impermeable boundaries along the meridional axis (y) and periodic boundaries along the zonal axis (x). Key parameters encompass a constant Coriolis parameter set at -1.2 $\times$ 10^{-4} $s^{-}1$, quadratic bottom drag coefficient of 0.01 and a density function formulated from temperature variations.

Algorithm 2: split IMEX iteration for the hydrodynamic equations, $m = M/2$

Data: Model state variable $\mathbf{u}, z$

$\mathbf{U}, H \leftarrow \sum_z \frac{h}{2}\mathbf{u}, \sum_z \frac{h}{2}$

$\mathbf{u}_0, h_0 \leftarrow \mathbf{u}, h$

$\mathbf{U}_0, H_0 \leftarrow \mathbf{U}, H$

First sub-time step

$\mathbf{f}^{\mathrm{xy}} \leftarrow f_{3d}^{\mathrm{xy}}(\mathbf{u}, z)$

$\mathbf{f}^{\mathrm{z1}} \leftarrow f_{3d}^{\mathrm{z1}}(\mathbf{u}, z)$

$\mathbf{u}^* \leftarrow M_{3d}^{-1}\left(M_{3d}^0\mathbf{u}_0 + \frac{\Delta t}{2}\left(\mathbf{f}^{\mathrm{xy}} + f_{3d}^{\mathrm{z0}}(\mathbf{u}^*, z) + \mathbf{f}_{3d}^{\mathrm{z1}}\mathbf{u}^*\right)\right)$

$\mathbf{f}^{\mathrm{z0}} \leftarrow f_{3d}^{\mathrm{z0}}(\mathbf{u}^*, z)$

$\mathbf{F}^{\mathrm{xy}} \leftarrow \sum_z \mathbf{f}^{\mathrm{xy}}$

$\mathbf{F}^{\mathrm{z0}} \leftarrow \sum_z \mathbf{f}^{\mathrm{z0}}$

$\mathbf{F}^{\mathrm{z1}}\mathbf{U} \leftarrow \sum_z \mathbf{f}^{\mathrm{z1}}\mathbf{u}^*$

$\mathbf{U}, H \leftarrow \mathbf{U}_0, H_0$

$\mathbf{F}^{\mathrm{fast}} \leftarrow 0$

for *j=1,...,m* **do**

  $\mathbf{F}_{\mathbf{U}}, F_H \leftarrow F_{2d}(\mathbf{U}, H)$

  $\mathbf{F}_{\mathbf{U}}, F_H \leftarrow F_{2d}(\mathbf{U} + \frac{\Delta T}{2}M_{2d}^{-1}(\mathbf{F}_{\mathbf{U}} + \mathbf{F}^{\mathrm{xy}} + \mathbf{F}^{\mathrm{z0}} + \mathbf{F}^{\mathrm{z1}}\mathbf{U}), H + \frac{\Delta T}{2}M_{2d}^{-1}F_H)$

  $\mathbf{U} \leftarrow \mathbf{U} + \Delta T M_{2d}^{-1}(\mathbf{F}_{\mathbf{U}} + \mathbf{F}^{\mathrm{xy}} + \mathbf{F}^{\mathrm{z0}} + \mathbf{F}^{\mathrm{z1}}\mathbf{U})$

  $H \leftarrow H + \Delta T M_{2d}^{-1}F_H$

  $\mathbf{F}^{\mathrm{fast}} \leftarrow \mathbf{F}^{\mathrm{fast}} + \Delta T\mathbf{F}_{\mathbf{U}}$

Update the z coordinates based on H

$\mathbf{u}_{n+\frac{1}{2}} \leftarrow M_{3d}^{-1}\left(M_{3d}^0\mathbf{u}_0 + \frac{\Delta t}{2}\left(\mathbf{f}^{\mathrm{xy}} + f_{3d}^{\mathrm{z0}}(\mathbf{u}_{n+\frac{1}{2}}, z) + \mathbf{f}^{\mathrm{z1}}\ \mathbf{u}_{n+\frac{1}{2}}\right) + \frac{1}{2}\frac{h}{H}\mathbf{F}^{\mathrm{fast}}\right)$

Second sub-time step

$\mathbf{f}^{\mathrm{xy}} \leftarrow f_{3d}^{\mathrm{xy}}(\mathbf{u}_{n+\frac{1}{2}}, z)$

$\mathbf{f}^{\mathrm{z0}} \leftarrow f_{3d}^{\mathrm{z0}}(\mathbf{u}_{n+\frac{1}{2}}, z)$

$\mathbf{f}^{\mathrm{z1}} \leftarrow f_{3d}^{\mathrm{z1}}(\mathbf{u}_{n+\frac{1}{2}}, z)$

$\mathbf{F}^{\mathrm{xy}} \leftarrow \sum_z \mathbf{f}^{\mathrm{xy}}$

$\mathbf{F}^{\mathrm{z0}} \leftarrow \sum_z \mathbf{f}^{\mathrm{z0}}$

$\mathbf{F}^{\mathrm{z1}}\mathbf{U} \leftarrow \sum_z \mathbf{f}^{\mathrm{z1}}\mathbf{u}_{n+\frac{1}{2}}$

$\mathbf{U}, H \leftarrow \mathbf{U}_0, H_0$

$\mathbf{F}^{\mathrm{fast}} \leftarrow 0$

for *j=1,...,2m* **do**

  $\mathbf{F}_{\mathbf{U}}, F_H \leftarrow F_{2d}(\mathbf{U}, H)$

  $\mathbf{F}_{\mathbf{U}}, F_H \leftarrow F_{2d}(\mathbf{U} + \frac{\Delta T}{2}M_{2d}^{-1}(\mathbf{F}_{\mathbf{U}} + \mathbf{F}^{\mathrm{xy}} + \mathbf{F}^{\mathrm{z0}} + \mathbf{F}^{\mathrm{z1}}\mathbf{U}), H + \frac{\Delta T}{2}M_{2d}^{-1}F_H)$

  $\mathbf{U} \leftarrow \mathbf{U} + \Delta T M_{2d}^{-1}(\mathbf{F}_{\mathbf{U}} + \mathbf{F}^{\mathrm{xy}} + \mathbf{F}^{\mathrm{z0}} + \mathbf{F}^{\mathrm{z1}}\mathbf{U})$

  $H \leftarrow H + \Delta T M_{2d}^{-1}F_H$

  $\mathbf{F}^{\mathrm{fast}} \leftarrow \mathbf{F}^{\mathrm{fast}} + \Delta T\mathbf{F}_{\mathbf{U}}$

Update the z coordinates based on H

$\mathbf{u}_{n+1} \leftarrow M_{3d}^{-1}\left(M_{3d}^0\mathbf{u}_0 + \Delta t\left(\mathbf{f}^{\mathrm{xy}} + \mathbf{f}^{\mathrm{z0}} + \mathbf{f}^{\mathrm{z1}}\ \mathbf{u}_{n+\frac{1}{2}}\right) + \frac{1}{2}\frac{h}{H}\mathbf{F}^{\mathrm{fast}}\right)$

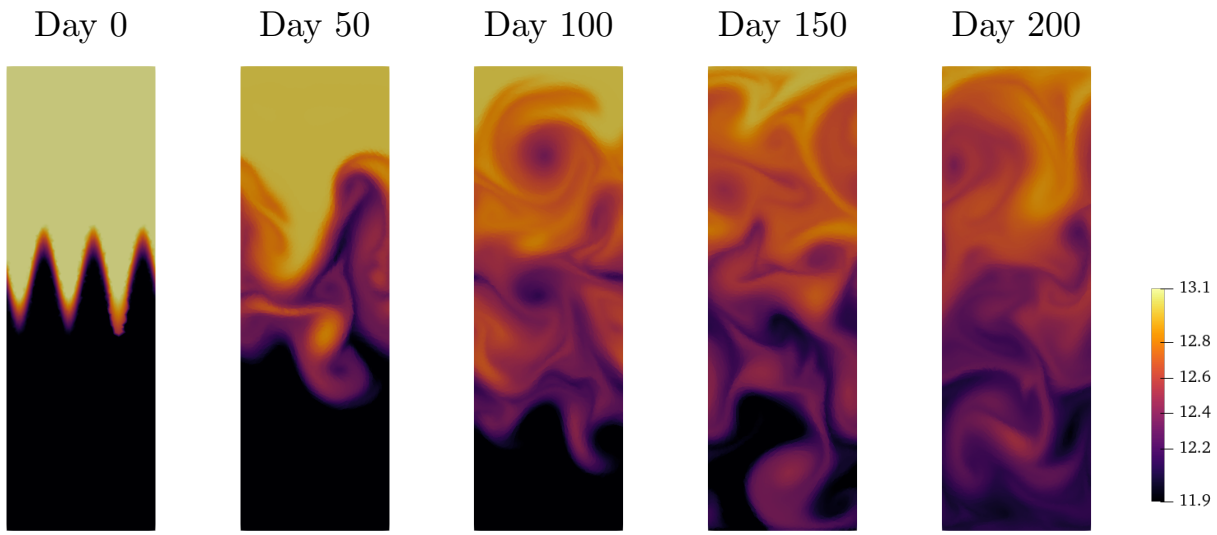

Figure 4: Sea surface temperature field [°C] of the baroclinic eddies test case for 200 days with the split IMEX Runge-Kutta. The horizontal viscosity is 20 m^2/s.

Its expression is given by

$$\rho(x, y, z) = 1000 - 0.2(T(x, y, z) - 5)$$

where T is the temperature in °C. The initial temperature distribution is given by Ilıcak et al. (2012).

This simulation employs a 4 km horizontal grid resolution coupled with a horizontal viscosity of 20 m^2/s. In Figure 4, The simulation showcases the initial temperature field, with warmer northern and colder southern surface temperatures separated by a sinusoidal transition band. The evolution of sea surface temperature over time further underscores the model's proficiency in capturing and reproducing mesoscale features, particularly evident when reducing viscosity while considering rotational influences.

Furthermore, the mixing during this test case is quantified by computing the Resting Potential Energy (RPE) Ilıcak et al. (2012); Petersen et al. (2015). This metric measures the portion of potential energy lost due to the mixing of waters with different densities. It is defined from a sorted density field ρ^*:

$$RPE = \int g\rho^* z \, d\mathbf{X}$$

The density field ρ^* is obtained by sorting the prisms in increasing order of density and distributing them from the top to the bottom of the domain, with the densest prisms at the bottom. For the eddies test case, the prisms are sorted and distributed over a vertical range from 0 to -1000 m. Each prism retains its volume and the new horizontal area of the prisms is the horizontal surface of the domain. Consequently, the new average height of the prisms is obtained by dividing their volume by this area.

RPE represents the potential energy that can no longer be converted back into kinetic energy. Since the initial value of RPE in a simulation depends on the domain and initial conditions, it is not relevant to the mixing. Therefore, the RPE values are normalized to time zero:

$$\text{Relative } RPE = \frac{RPE(t) - RPE(0)}{RPE(0)}$$

Figure 5 shows the evolution of the relative RPE during the simulation for $\nu_h = 20$ m^2/s and $\nu_h = 200$ m^2/s over 320 days. The curves are in good agreement with Petersen et al. (2015); Kärnä et al. (2018). They increase monotonically in the same manner. Increasing the horizontal viscosity results in lower relative RPE values. However, compared to them, for the same ν_h, the proposed model produces higher values.

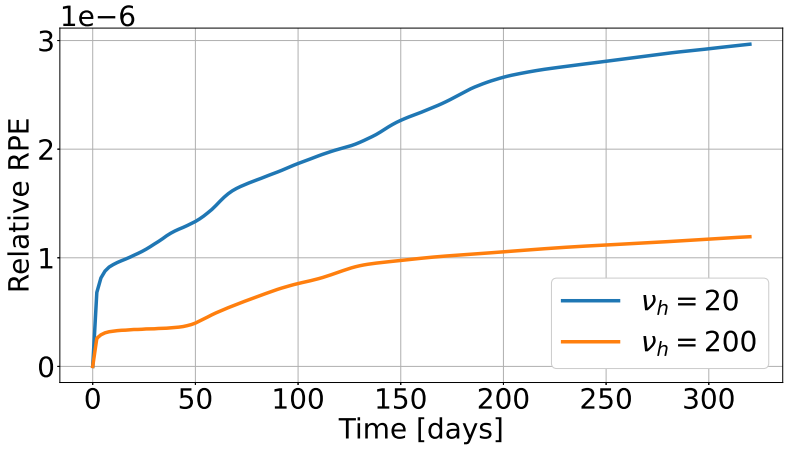

Figure 5: Relative RPE of the baroclinic eddies test case for 320 days with the split IMEX Runge-Kutta.

This suggests that the model mixes waters of different densities more effectively. Due to the low numerical diffusion of our model, the relative RPE value at 320 days with $\nu_h = 200\ m^2/s$ matches more or less the ones obtained by Kärnä et al. (2018) with $\nu_h = 20\ m^2/s$ and Petersen et al. (2015) with $\nu_h = 1\ m^2/s$.

Additionally, a convergence analysis of the temporal scheme is done in Figure 6. The error is computed with the L_2 norm as follows

$$E = \|f - f^{ref}\|_{L_2} = \sqrt{\int_\Omega (f - f^{ref})^2 d\Omega}$$

with f the variable of interest and f^{ref} the reference solution. The simulation is running for 2000 s with the following set of Δt : [200, 100, 50, 25, 1.25] s and M=138. The solution obtained with the smallest time resolution is used as a reference. The order of accuracy is obtained by computing the slope of the error versus the time step. The slope is 2.0 which confirms the second-order accuracy of the scheme.

Finally, let us consider the eddies test case with a traditional non-split second-order Runge-Kutta scheme. In other words, the entire set of equations is solved as one system using the same time step. For stability, running this test case with a non-split scheme requires using the time step size appropriate for the 2D terms for all terms. This time step is 138 times smaller than the time step for the 3D terms (M=138). Additionally, in this simulation, evaluating the 3D terms is 700 times more computationally expensive than evaluating the 2D terms. Therefore, the duration of a complete iteration in a non-split scheme is primarily dictated by the time required for the 3D terms. Taking into account the time for the 2D iterations as well as communications, executing the split temporal scheme would take $M/2$ less time than the second-order Runge-Kutta scheme for the entire system for the eddies test case. In practice, the split temporal scheme takes about 1050 seconds to reach 200 days. For the classic non-split RK scheme, during this time, the simulation only progresses to about 2.7 days. The split scheme is 73.5 times faster.

4.2. Dynamics of Overflow Mixing and Entrainment

The following test case is known as the Dynamics of Overflow Mixing and Entrainment, or DOME, test case (Ezer and Mellor (2004); Legg et al. (2006); Wang et al. (2008); Burchard and Rennau (2008); Reckinger et al. (2015)). This test aims to evaluate the method's performance in generating swirling patterns. The fluid flow is primarily influenced by gravity and the Coriolis effect. It serves as a simplified representation of the Denmark Strait overflow. In a stratified basin, dense water is introduced through a channel. Through a passive tracer, the movement of the water can be tracked.

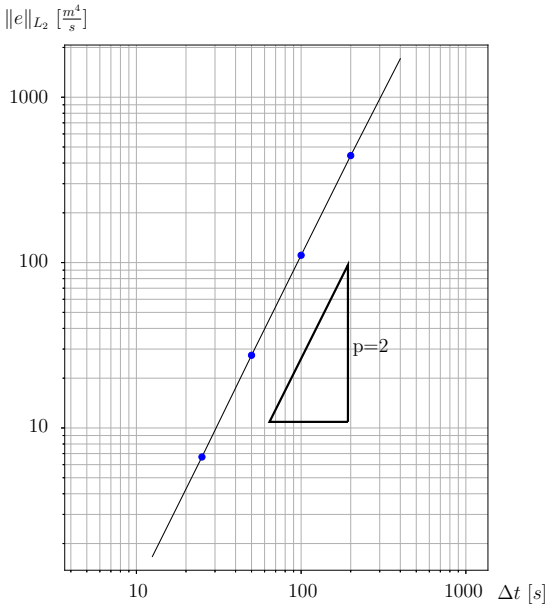

Figure 6: Error convergence of the baroclinic eddies test case with the split IMEX Runge-Kutta. The expected slope of two is shown for reference.

The domain is a rectangular box measuring 1100 km in length and 600 km in width. The bathymetry is constant at 3600 m between x = 0 and x = 300 km. Then, it transitions to a slope, decreasing from 3600 m to 600 m between x = 300 km and x = 600 km. Finally, a 100 × 200 km channel is located at the northern part of the domain. Concerning boundary conditions, the eastern, southern and western boundaries are open with an elevation of 0 m. At the northern part of the channel, it is also open but additionally, along with a zero elevation, an incoming velocity with a maximum value of 0.75 ms^{-1} is applied, whose equation will be described later. The rest of the boundaries are closed. Figure 8 illustrates the domain.

The 3D grid is created from a horizontal grid illustrated in Figure 7 with a characteristic size of 5 km and contains 20 vertical layers, resulting in a horizontal mesh Reynolds number of 200.

Regarding temperature, initially, it varies between 10 and 20 degrees Celsius, with 10 degrees at the bottom of the basin and 20 degrees at the surface. The incoming water has a temperature mostly of 10 degrees. This equation is also described later. For the passive tracer, its concentration is 0 within the domain and 1 at the entrance of the channel, ensuring it represents an image of the velocity field. The Coriolis parameter is taken as a constant 1×10^{-4} s^{-1}. The quadratic bottom drag coefficient is $2e^{-}3$. The horizontal viscosity and diffusivity are 18.75 m^2s^{-1} and 10 m^2s^{-1} respectively. The vertical viscosity and diffusivity are 0.1875 m^2s^{-1} and 0 m^2s^{-1} respectively.

The state equation of the density and the temperature field are given by

$$\rho(z) = \rho_0 - 0.2(T(z) + 10)$$
$$T(z) = \frac{z}{360} + 20$$

with ρ_0 the reference density and z the vertical coordinate.

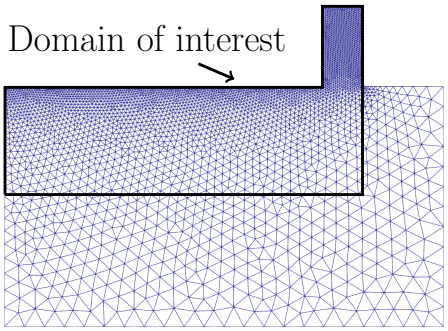

Figure 7: Horizontal mesh of the DOME test case. The characteristic size at the entry is 5 km then becomes 50 km which produces 7234 triangles.

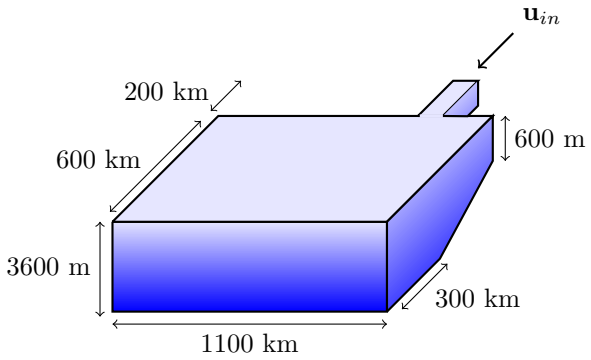

Figure 8: Geometry of the DOME test case. The blue color represents the vertical gradient in density field. The arrow represents the incoming flow. The canal is 100 km wide and 200 km long with a depth of 600 m.

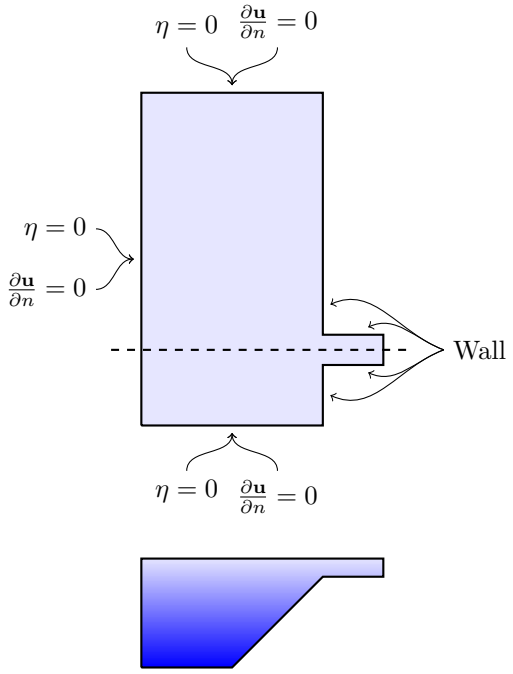

Figure 9: Boundary conditions of the DOME test case

For x_w, the distance from the wall at $x = 800$ km, the incoming velocity is given by

$$u_{in}(x_w, z) = -u_0 \exp\left(-\frac{x_w f}{u_0}\right)(1 - F(z^*))$$

with u_0 the maximum incoming velocity, f the Coriolis parameter. $F(z^*)$ is the following function

$$F(z*) = \begin{cases} 1 & z^* \leq \frac{1}{5} \\ \frac{3z^*}{z^*+1} & -\frac{1}{6} < z^* \leq \frac{1}{5} \\ 0 & -\frac{1}{6} \leq z^* \end{cases}$$

with

$$z^* = \frac{z - h_0 \exp\left(-\frac{x_w f}{u_0}\right) - h_e}{h_0 \exp\left(-\frac{x_w f}{u_0}\right)}$$

where h_0 is the depth of the incoming flow set at 300 m and h_e the depth of the channel set at 600 m.

The incoming fluid temperature is given by

$$T_{in}(z) = \frac{10}{\Delta b_0} \min\left(-\Delta b_0 \left(1 - F(z), 0\right)\right) + 20$$

with Δb_0 the maximum buoyancy difference between the incoming fluid and the ambient fluid.

Finally, the maximum velocity, u_0, is set by the following equation

$$u_0 = \sqrt{h_0 \Delta b_0}$$

The simulation is run for 40 days with a time step of 60 s and a factor M of 30. The results can be seen in Figure 10. This is the evolution of the passive tracer in last layer. As the current flows into the basin, it derives westward, forming a coastal plume spanning about 150 km in width. This plume separates from the side boundary, continuing its westward journey along the bottom slope. Upon encountering the stratified ocean, this dense water mass becomes unstable, leading to the formation of swirling eddies and internal waves. The most robust eddies occur within the initial 300 km after the inlet (x = 500–800 km). Beyond this range, the plume becomes more mixed and less turbulent. The plume remains relatively shallow, with the majority of the passive tracer concentrated within 200 meters of the bottom. In terms of its extent, movement and eddy patterns, the results are in good agreement with the results of Wang et al. (2008).

Furthermore, the eastward transport within the plume in the along-slope direction is used to quantify the mixing Reckinger et al. (2015). The transport is computed by integrating the velocity field in the y and z directions. The temporal-averaged transport is computed from all time steps. The integral only looks at the $y - z$ cross ection where the passif tracer is higher than 0.01. This gives the following equation for the eastward transport:

$$U_{yz} = \int_A u(x, y, z)\, dy\, dz \tag{25}$$

where A is the area where the passive tracer is higher than 0.01. Figure 11 shows the temporal-averaged eastward transport for x between 0 and 800 km. The transport is negative as the plume is moving westward. The highest negative value is at $x = 400$ km. At $x = 800$ km, the value is close to -1×10^7 m^3/s. The U_{yz} values tend to not change a lot until $x = 100$ km. After that, the values reaches 0 at $x = 0$ km.

Concerning the performances, running this test case with a second-order non-split scheme results in a simulation that is approximately 16 times slower. This aligns logically with the value of M.

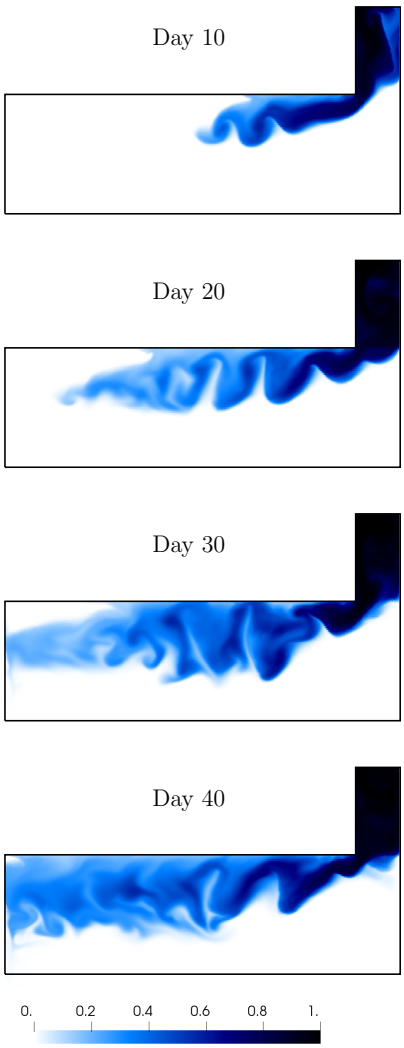

Figure 10: Evolution of the passive tracer concentration in the bottom layer for the DOME test case. The maximum value of u_{in} is 0.75 ms^{-1}. The horizontal viscosity is 18.75 m^2s^{-1}. We have successive snapshots of the passive tracer concentration at 10, 20, 30, 40 days.

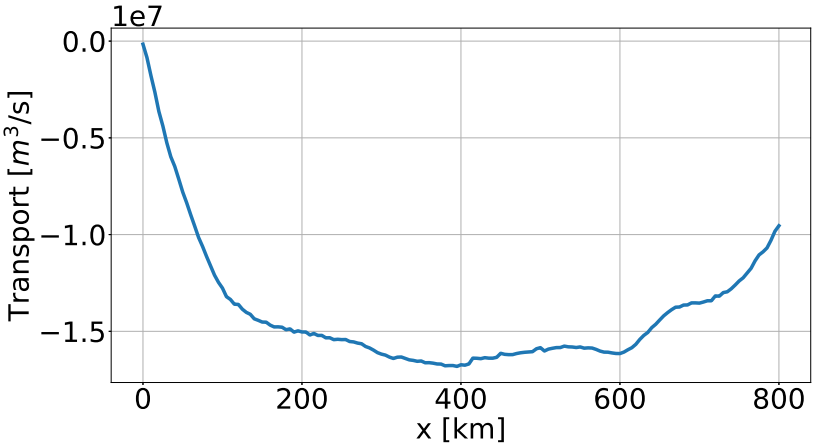

Figure 11: Temporal-averaged eastward transport of the DOME test case for 40 days with the split IMEX Runge-Kutta.

5. Conclusion

This study introduces an innovative split Implicit-Explicit temporal scheme of order 2 specifically designed to tackle the complexities ODE equations characterized by three distinct timescales. The main goal of this approach is to limit numerical dissipation due to temporal discretization. This temporal scheme is tailored for equations with extremely stiff terms that are computationally inexpensive. Its semi-implicit aspect specifically targets equations with a high aspect ratio, where the vertical characteristic length is much smaller than the horizontal one. These equations tend to have a more restrictive vertical Courant-Friedrichs-Lewy constraint. For instance, this is applicable to atmospheric or oceanic problems.

This IMEX scheme has undergone extensive theoretical analysis to verify its second-order convergence and assess its stability across diverse scenarios, demonstrating its reliability and robustness in computational simulations.

The application of the IMEX scheme extends to solving intricate 3D hydrodynamic equations, subjecting it to test cases such as Baroclinic Eddies and DOME simulations. These tests serve as empirical evidence of the scheme's exceptional accuracy and computational efficiency in mimicking the complex fluid dynamics observed in oceanic phenomena.

The IMEX scheme, a noteworthy addition to oceanic modeling, stands as a groundbreaking tool capable of accurately capturing ocean behaviors across multiple timescales. Its adeptness in handling intricate dynamics while ensuring computational efficiency signifies a significant progress forward in the realm of oceanic simulations

6. Acknowledgements

Computational resources were provided by the Consortium des Équipements de Calcul Intensif (CÉCI), funded by the Belgian Fund for Scientific Research (F.R.S. FNRS) under grant no. 2.5020.11

Appendix A. Spatial discretization

To achieve spatial discretization, the continuous equations are multiplied by shape functions. For the 2D equations, the shape function $\phi_i(x, y)$ is used, while for the 3D equations, $\phi_i(x, y, z)$ is applied. The 2D equations are discretized using discontinuous bilinear functions, whereas the 3D equations are discretized with discontinuous functions that combine bilinear horizontal functions with linear vertical functions. These equations are then integrated by parts, resulting in volume terms and flux terms.

The following notations are used:

$$\left\langle \bullet \right\rangle = \int_{\Omega} \bullet \mathrm{d}V$$
$$\left\langle\left\langle \bullet \right\rangle\right\rangle_{\partial\Gamma_h} = \int_{\partial\Gamma_h} \bullet \mathrm{d}S$$
$$\left\langle\left\langle \bullet \right\rangle\right\rangle_{\partial\Gamma_v} = \int_{\partial\Gamma_v} \bullet \mathrm{d}S$$

Ω represents the domain while $\partial\Gamma$ represents the interfaces. In 2D, Ω represents the horizontal triangles and the interfaces are the edges. In 3D, Ω represents the prisms. $\partial\Gamma_h$ and $\partial\Gamma_v$ correspond to the horizontal and vertical interfaces.

The hydrodynamic equation includes both 3D and 2D terms. The 2D terms, which represent the fast processes, are separated, creating two distinct function spaces: one for 2D and another for 3D. In the integrals at the interfaces, an average value is applied to the terms involving horizontal velocities. $\{\cdot\}$ represents the mean operator :

$$\{\mathbf{u}\cdot\mathbf{n}_h\} = \frac{\mathbf{u}_{right}\cdot\mathbf{n}_h + \mathbf{u}_{left}\cdot\mathbf{n}_h}{2}$$
$$\{w\} = \frac{w_{right} + w_{left}}{2}$$

where $\mathbf{u}_{right}, w_{right}$ and $\mathbf{u}_{left}, w_{left}$ are the velocities on the right and left sides of the interface, respectively. In the vertical interfaces integrals, an upwind term is used, $\mathbf{u}^{up}$. The discretization of the hydrodynamic equation is as follows:

$$\left\langle \phi_i \frac{\partial \mathbf{u}}{\partial t} \right\rangle = f_{3d}(\mathbf{u}) + \frac{1}{H} f_{2d}(H\mathbf{u}) \tag{26}$$

with

$$\begin{aligned} f_{2d}(H\mathbf{u}) =& \left\langle g\frac{H^2}{2}\boldsymbol{\nabla}_h\cdot\boldsymbol{\phi}_i \right\rangle - \left\langle\left\langle g\left(\frac{H_{left}^2 + H_{right}^2}{4}\right)\boldsymbol{\phi}_i\cdot\mathbf{n}\right\rangle\right\rangle \\ &+ \left\langle \phi_i g(1+\frac{\rho'|_\eta}{\rho_0})H\boldsymbol{\nabla}_h b\right\rangle + \left\langle \frac{g}{\rho_0}\frac{H^2}{2}\boldsymbol{\nabla}_h\left(\rho'|_\eta\right)\phi_i\right\rangle \\ f_{3d}(\mathbf{u}) =& \left\langle \mathbf{u}\mathbf{u}\cdot\boldsymbol{\nabla}_h\phi_i\right\rangle - \left\langle\left\langle \phi_i\mathbf{u}^{up}\left\{\mathbf{u}\cdot\mathbf{n}_h\right\}\right\rangle\right\rangle_{\Gamma_h\cup\Gamma_v} + \left\langle w\mathbf{u}\frac{\partial\phi_i}{\partial z}\right\rangle \\ &- \left\langle\left\langle \phi_i\left\{w\right\}\mathbf{u}^{up}n_z\right\rangle\right\rangle_{\Gamma_h} - \left\langle \phi_i\mathbf{f}\times\mathbf{u}\right\rangle - \left\langle\phi_i\mathbf{q}\right\rangle + \text{Diffusion} \end{aligned}$$

The diffusive terms have been omitted for the sake of clarity.

Unlike the horizontal velocities mentioned earlier, H is a 2D variable, so 2D function spaces are used. To the interface integrals, stabilization terms are introduced using the Lax-Friedrichs approximate solver. For $i = 1, \ldots, n$, this results in:

$$\left\langle \phi_i\frac{\partial H}{\partial t}\right\rangle = \left\langle \mathbf{U}\cdot\boldsymbol{\nabla}_h\phi_i\right\rangle - \left\langle\left\langle \phi_i\mathbf{U}^*\cdot\mathbf{n}_h\right\rangle\right\rangle \tag{27}$$

with

$$\mathbf{U}^* = \frac{(\mathbf{U}_{left} + \mathbf{U}_{right}) \cdot \mathbf{n}_h}{2} - c\frac{(\eta_{left} - \eta_{right})}{2}$$
$$c = \max\left(\sqrt{gH_{left}} + \left|\left|\frac{\mathbf{U}_{n,left}}{H_{left}}\right|\right|, \sqrt{gH_{right}} + \left|\left|\frac{\mathbf{U}_{n,right}}{H_{right}}\right|\right)$$

Finally, the vertical velocity equation becomes

$$-\left\langle \frac{\partial \phi_i}{\partial z} w \right\rangle + \left\langle \left\langle \phi_i \left\{w\right\} n_z \right\rangle \right\rangle_{\Gamma_h} = \left\langle \mathbf{u} \cdot \boldsymbol{\nabla}_h \phi_i \right\rangle - \left\langle \left\langle \phi_i \left\{\mathbf{u} \cdot \mathbf{n}_h\right\} \right\rangle \right\rangle_{\Gamma_h \cup \Gamma_v} \tag{28}$$

The spatial discretization of the temperature, salinity, or any scalar field equation is derived in a similar manner.

References

Blaise, S., Comblen, R., Legat, V., Remacle, J., Deleersnijder, E., Lambrechts, J., 2010. A discontinuous finite element baroclinic marine model on unstructured prismatic meshes. Ocean Modelling 60, 1371–1393. URL: https://doi.org/10.1007/s10236-010-0358-3.

Blaise, S., Deleersnijder, E., White, L., Remacle, J., 2007. Influence of the turbulence closure scheme on the finite element simulation of the upwelling in the wake of a shallow-water island. Continental Shelf Research 27, 2329–2345. URL: https://doi.org/10.1016/j.csr.2007.06.003.

Blumberg, A., Mellor, G., 1987. A description of a three-dimensional coastal ocean model, in: Three dimensional coastal ocean models. American Geophysical Union 69, 1–16. URL: https://doi.org/10.1029/CO004p0001.

Burchard, H., 2002. Energy-conserving discretization of turbulent shear buyouancy production. Ocean Modelling 4, 347–361. URL: https://doi.org/10.1016/S1463-5003(02)00009-4.

Burchard, H., Deleersnijder, E., Meister, A., 2003. A high-order conservative patankar-type discretisation for stiff systems of production–destruction equations. Applied Numerical Mathematics 47, 1–30. URL: https://doi.org/10.1016/S0168-9274(03)00101-6.

Burchard, H., Rennau, H., 2008. Comparative quantification of physically and numerically induced mixing in ocean models. Ocean modelling 20, 293–311. URL: https://doi.org/10.1016/j.ocemod.2007.10.003.

Canuto, V.M., Howard, A., Cheng, Y., Dubovikov, M.S., 2001. Ocean turbulence. part i: One-point closure model - momentum and heat vertical diffusivities. Journal of Physical Oceanography 31, 1413–1426. URL: https://doi.org/10.1175/1520-0485(2001)031.

Clare, M.C.A., Wallwork, J.G., Kramer, S.C., Weller, H., Cotter, C.J., Piggott, M.D., 2022. Multi-scale hydro-morphodynamic modelling using mesh movement methods. International Journal on Geomathematics 13 (2), 1869–2680. URL: https://doi.org/10.1007/s13137-021-00191-1.

Comblen, R., Blaise, S., Legat, V., Remacle, J., Deleersnijder, E., Lambrechts, J., 2010. A discontinuous finite element baroclinic marine model on unstructured prismatic meshes. Ocean Modelling 60, 1395–1414. URL: https://doi.org/10.1007/s10236-010-0357-4.

Danilov, S., 2013. Ocean modelling on unstructured meshes. Ocean Modelling 69, 195–210. URL: https://doi.org/10.1016/j.ocemod.2013.05.005.

Danilov, S., Wang, Q., Losch, M., Sidorenko, D., Schröter, J., 2008. Modeling ocean circulation on unstructured meshes: comparison of two horizontal discretizations. Ocean modelling 58, 365–374. URL: https://doi.org/10.1007/s10236-008-0138-5.

Deleersnijder, E., Lermusiaux, P., 2008. Multi-scale modelling: Nested grid and unstructured mesh approaches. Ocean modelling 58, 335–498. URL: https://doi.org/10.1007/s10236-008-0170-5.

Ezer, T., Mellor, G.L., 2004. A generalized coordinate ocean model and a comparison of the bottom boundary layer dynamics in terrain-following and in z-level grids. Ocean Modelling 6, 379–403. URL: https://doi.org/10.1016/S1463-5003(03)00026-X.

Formaggia, L., Nobile, F., 2004. Stability analysis of second-order time accurate schmes for ALE-FEM. Computer Methods in Applied Mechanics and Engineering 193, 4097–4116. URL: https://doi.org/10.1016/j.cma.2003.09.028.

Griffies, S.M., Gnanadesikan, A., Dixon, K.W., Dunne, J.P., Gerdes, R., Harrison, M.J., Rosati, A., Russell, J.L., Samuel, B.L., Spelman, M.J., Winton, M., Zhang, R., 2005. Formulation of an ocean model for global climate simulations. Ocean modelling 1, 45–79. URL: https://doi.org/10.5194/os-1-45-2005.

Griffies, S.M., Pacanowski, R.C., Hallberg, R.W., 2000. Spurious diapycnal mixing associated with advection in a z-coordinate ocean model. Monthly Weather Review 128, 538–564. URL: https://doi.org/10.1175/1520-0493(2000)128%3C0538:SDMAWA%3E2.0.CO;2.

Hiester, H., Piggot, M., Farrell, P., Allison, P., 2014. Assessment of spurious mixing in adaptive mesh simulations of the two-dimensional lock-exchange. Ocean modelling 73, 30–44. URL: https://doi.org/10.1016/j.ocemod.2013.10.003.

Ilıcak, M., Adcroft, A.J., Griffies, S.M., Hallberg, R.W., 2012. Spurious dianeutral mixing and the role of momentum closure. Ocean Modelling 45–46, 37–58. URL: https://doi.org/10.1016/j.ocemod.2011.10.003.

Isgin, T., Ranocha, H., 2023. Using bayesian optimization to design time step size controllers with application to modified patankar–runge–kutta methods URL: https://doi.org/10.48550/arXiv.2312.01796, arXiv:2312.01796.

Ishimwe, A.P., Deleersnijder, E., Legat, V., Lambrechts, J., 2023. A split-explicit second order Runge–Kutta method for solving 3D hydrodynamic equations. Ocean Modelling 186. URL: https://doi.org/10.1016/j.ocemod.2023.102273.

Jackett, D.R., McDougall, T.J., Feistel, R., Wright, D.G., Wright, S.M., 2006. Algorithms for density, potential temperature, conservative temperature, and the freezing temperature of seawater. Journal of Atmospheric and Oceanic Technology 23, 1709–1728. URL: https://doi.org/10.1175/JTECH1946.1.

Kärnä, T., Kramer, S.C., Mitchell, L., Ham, D.A., Piggot, M.D., Baptista, A.M., 2018. Thetis coastal ocean model: discontinuous Galerkin discretization for the three-dimensional hydrostatic equations. Geoscientific Model Development 1, 4359–4382. URL: https://doi.org/10.5194/gmd-11-4359-2018.

Kärnä, T., Legat, V., Deleersnijder, E., 2013. A baroclinic discontinuous Galerkin finite element model for coastal flows. Ocean Modelling 61, 1–20. URL: https://doi.org/10.1016/j.ocemod.2012.09.009.

Knoth, O., Wensch, J., 2003. On the convergence rate of operator splitting for advection–diffusion–reaction problems. SIAM Journal on Numerical Analysis 41, 1–24.

Kopecz, S., Meister, A., 2018. On order conditions for modified patankar–runge–kutta schemes. Applied Numerical Mathematics 123, 159–179. URL: https://doi.org/10.1016/j.apnum.2017.09.004.

Kärnä, T., 2020. Discontinuous galerkin discretization for two-equation turbulence closure model. Ocean Modelling 150. URL: https://doi.org/10.1016/j.ocemod.2020.101619.

Large, W.G., McWilliams, J.C., Doney, S.C., 1994. Oceanic vertical mixing: A review and a model with a nonlocal boundary layer parameterization. Reviews of Geophysics 32, 363–403. URL: https://doi.org/10.1029/94RG01872.

Legg, S., Hallberg, R.W., Girton, J.B., 2006. Comparison of entrainment in overflows simulated by z-coordinate, isopycnal and non-hydrostatic models. Ocean Modelling 11, 69–97. URL: https://doi.org/10.1016/j.ocemod.2004.11.006.

Marchesiello, P., Debreu, L., Couvelard, X., 2009. Spurious diapycnal mixing associated with advection in terrain-following coordinate models: The problem and a solution. Ocean Modelling 26, 156–169. URL: https://doi.org/10.1016/j.ocemod.2008.09.004.

Mellor, G.L., Yamada, T., 1982. Development of a turbulence closure model for geophysical fluid problems. Reviews of Geophysics 20, 851–875. doi:https://doi.org/10.1029/RG020i004p00851.

Nilsen, J.E.O., Loseth, O., 1993. A time-splitting method for the numerical simulation of the navier-stokes equations. Journal of Computational Physics 109, 1–32.

Pacanowski, R.C., Philander, S.G.H., 1981. Parameterization of vertical mixing in numerical models of tropical oceans. Journal of Physical Oceanography 11, 1443 – 1451. URL: https://doi.org/10.1175/1520-0485(1981)011<1443:POVMIN>2.0.CO;2.

Pan, W., Kramer, S.C., Piggott, M.D., 2019. Multi-layer non-hydrostatic free surface modelling using the discontinuous galerkin method. International Journal on Geomathematics 134, 68–83. URL: https://doi.org/10.1016/j.ocemod.2019.01.003.

Pan, W., Kramer, S.C., Piggott, M.D., 2021. A sigma-coordinate non-hydrostatic discontinuous finite element coastal ocean model. Ocean Modelling 157, 1463–5003. URL: https://doi.org/10.1016/j.ocemod.2020.101732.

Patankar, S., 1980. Numerical Heat Transfer and Fluid Flow. McGraw-Hill. URL: https://doi.org/10.1201/9781482234213.

Petersen, M., Jacobsen, D., Ringler, T., Hecht, M., Maltrud, M., 2015. Evaluation of the arbitrary Langrangian-Eulerian vertical coordinate method in the MPAS-ocean model. Ocean Modelling 86, 93–113. URL: https://doi.org/10.1016/j.ocemod.2014.12.004.

Pigott, M.D., Pain, C.C., Gorman, G.J., Marshall, D.P., Killworth, P.D., 2013. nstructured adaptive meshes for ocean modeling. American Geophysical Union 177, 383–108. URL: https://doi.org/10.1029/177GM22.

Reckinger, S., Petersen, M., Reckinger, S., 2015. A study of overflow simulations using mpas-ocean: Vertical grids, resolution, and viscosity. Ocean Modelling 96, 291–313. URL: https://doi.org/10.1016/j.ocemod.2015.09.006.

Rennau, H., Burchard, H., 2009. Quantitative analysis of numerically induced mixing in a coastal model application. Ocean modelling 59, 671–687. URL: https://doi.org/10.1007/s10236-009-0201-x.

Robert, A.M., Kaper, H.G., 1986. Multiple time scale phenomena and numerical methods. Journal of computational physics 63, 241–256.

Rodi, W., 1987. Examples of calculation methods for flow and mixing in stratified fluids. Journal of Geophysical Research 92, 5305–5328. URL: https://doi.org/10.1029/JC092iC05p05305.

Roekel, L.V., Adcroft, A.J., Danabasoglu, G., Griffies, S.M., Kauffman, B., Large, W., Levy, M., Reichl, B.G., Ringler, T., Schmidt, M., 2018. The kpp boundary layer scheme for the ocean: Revisiting its formulation and benchmarking one-dimensional simulations relative to les. Journal of Advances in Modeling Earth Systems 10, 2647–2685. URL: https://doi.org/10.1029/2018MS001336.

Shchepetkin A.F., M.J., 2005. The regional oceanic modeling system (ROMS) a split-explicit, free-surface, topography-following-coordinate oceanic model. Ocean Modelling 9, 347–404. URL: https://doi.org/10.1016/j.ocemod.2004.08.002.

Smagorinsky, J., 1963. General circulation experiments with the primitive equations: I. the basic experiment. Monthly Weather Review 91, 99–164. URL: https://doi.org/10.1175/1520-0493(1963)091<0099:GCEWTP>2.3.CO;2.

Song, Y., Haidvogel, D., 1994. A semi-implicit ocean circulation model using a generalized topography-following coordinate system. Journal of Computational Physics 115, 228–244. URL: https://doi.org/10.1006/jcph.1994.1189.

Umlauf, L., Burchard, H., 2003. A generic length-scale equation for geophysical turbulence models. Journal of Marine Systems 61, 235–265. URL: https://doi.org/10.1357/002224003322005087.

Visbal, M.R., Gaitonde, D.V., 2002. A study of numerical dissipation in time-splitting methods for navier–stokes equations. Journal of Computational Physics 177, 1–29.

Wang, Q., Danilov, S., Schröer, J., 2008. Comparison of overflow simulations on different vertical grids using the finite element ocean circulation model. Ocean Modelling 20, 313–335. URL: https://doi.org/10.1016/j.ocemod.2007.10.005.

Wensch, J., Knoth, O., Galant, A., 2009. Multirate infinitesimal step methods for atmospheric flow simulation. BIT Numerical Mathematics 49, 449–473. URL: https://doi.org/10.1007/s10543-009-0222-3.

White, L., Legat, V., Deleersnijder, E., 2008. Three-dimensional unstructured mesh finite element shallow-water model, with application to the flows around an island and in a wind-driven, elongated basin. Ocean Modelling 22, 22–47. URL: https://doi.org/10.1016/j.ocemod.2008.01.001.

Wicker, L.J., Skamarock, W.C., 2002. Time-splitting methods for elastic models using forward time schemes. Monthly Weather Review 130, 2088–2097.

Wilcox, D.C., 1988. Reassessment of the scale-determining equation for advanced turbulence models. AIAA Journal 26, 1299–1310. URL: https://doi.org/10.2514/3.10041.

Wilcox, D.C., 2008. Formulation of the k-w turbulence model revisited. AIAA Journal 46, 2823–2838. URL: https://doi.org/10.2514/1.36541, doi:10.2514/1.36541.

Zhang, Y., Ye, F., Stanev, E., Grashorn, S., 2016. Seamless cross-scale modeling with SCHISM. Ocean modelling 102, 64–81. URL: https://doi.org/10.1016/j.ocemod.2016.05.002.